



---

**This work was submitted at the  
Institute for Railway Vehicles and Transport Systems**

## **Master Thesis**

### **Validation of Finite Element Calculations of Wheel- Rail Normal Contact through DOE and Experiments**

Master Thesis

Ranganathan, Prasaenna

Matriculation number: 350861

Subject:

Validation of Finite Element Calculations of Wheel-Rail Normal Contact through DOE and Experiments

Abstract:

The aim of this thesis is to determine the shape and dimensions of contact patch that develop between a stationary wheel and rail and its corresponding pressure distribution using Finite Element Method (FEM). Previous studies show that wheel-rail contact is sensitive to input parameters. Thus, an empirical validation of the simulation is crucial. The challenge that one would face in FE modelling of this problem would be in the determination of input values, due to its ambiguous nature. For example, the Angle of inclination of the rail or lateral position of the wheel with respect to rail cannot be measured precisely. So, a tolerance value has to be added to these measured values. This also applies to other inputs like Force, Young's modulus and Poisson's ratio. Thus, we have multiple values for a single input. To help us with this problem, we take the help of Design of Experiments (DOE). DOE helps us not only to organize the inputs, but also to understand the effect of changes in inputs on output. It enables us to find out the best combination of input variables at which we get the desired contact patch.

## Eidesstattliche Versicherung

Ich versichere hiermit an Eides Statt, dass ich die vorliegende Master Thesis mit dem Titel

Validation of Finite Element Calculations of Wheel-Rail Normal Contact through DOE and Experiments

selbständig und ohne unzulässige fremde Hilfe erbracht habe. Ich habe keine anderen als die angegebenen Quellen und Hilfsmittel benutzt und die den benutzten Quellen wörtlich oder inhaltlich entnommenen Stellen als solche kenntlich gemacht.

Für den Fall, dass die Arbeit zusätzlich auf einem Datenträger eingereicht wird, erkläre ich, dass die schriftliche und die elektronische Form vollständig übereinstimmen. Die Arbeit hat in gleicher oder ähnlicher Form noch keiner Prüfungsbehörde vorgelegen.

---

Ort, Datum

---

Ranganathan, Prasaenna

### Belehrung:

#### **§ 156 StGB: Falsche Versicherung an Eides Statt**

Wer vor einer zur Abnahme einer Versicherung an Eides Statt zuständigen Behörde eine solche Versicherung falsch abgibt oder unter Berufung auf eine solche Versicherung falsch aussagt, wird mit Freiheitsstrafe bis zu drei Jahren oder mit Geldstrafe bestraft.

#### **§ 161 StGB: Fahrlässiger Falscheid; fahrlässige falsche Versicherung an Eides Statt**

(1) Wenn eine der in den §§ 154 bis 156 bezeichneten Handlungen aus Fahrlässigkeit begangen worden ist, so tritt Freiheitsstrafe bis zu einem Jahr oder Geldstrafe ein.

(2) Strafflosigkeit tritt ein, wenn der Täter die falsche Angabe rechtzeitig berichtigt. Die Vorschriften des § 158 Abs. 2 und 3 gelten entsprechend.

Die vorstehende Belehrung habe ich zur Kenntnis genommen:

---

Ort, Datum

---

Ranganathan, Prasaenna

The present translation is for your convenience only.  
Only the German version is legally binding

## Statutory Declaration in Lieu of an Oath

I hereby declare in lieu of an oath that I have completed the present Project Work / Bachelor Thesis / Master Thesis entitled

Title of the work

independently and without illegitimate assistance from third parties. I have use no other than the specified sources and aids. In case that the thesis is additionally submitted in an electronic format, I declare that the written and electronic versions are fully identical. The thesis has not been submitted to any examination body in this, or similar, form.

\_\_\_\_\_  
Aachen, Date

The German version has to be signed  
Ranganathan, Prasaenna

### Official Notification:

#### **Para. 156 StGB (German Criminal Code): False Statutory Declarations**

Whosoever before a public authority competent to administer statutory declarations, falsely makes such a declaration or falsely testifies while referring to such a declaration shall be liable to imprisonment not exceeding three years or a fine.

#### **Para. 161 StGB (German Criminal Code): False Statutory Declarations Due to Negligence**

(1) If a person commits one of the offences listed in sections 154 to 156 negligently the penalty shall be imprisonment not exceeding one year or a fine.

(2) The offender shall be exempt from liability if he corrects his false testimony in time. The provisions of section 158 (2) and (3) shall apply accordingly.

I have read and understood the above official notification:

\_\_\_\_\_  
Aachen, Date

The German version has to be signed  
Ranganathan, Prasaenna

# Table of contents

<b>List of abbreviations.....</b>	<b>III</b>
<b>List of symbols .....</b>	<b>IV</b>
<b>1 Introduction .....</b>	<b>1</b>
<b>2 Theoretical Basics .....</b>	<b>3</b>
2.1 The Wheel-Rail Interface .....	3
2.1.1 Geometry.....	3
2.1.2 Contact Mechanics .....	4
2.1.2.1 Frame of Reference .....	6
2.1.2.2 Hertz Theory for Elastic Bodies .....	8
2.2 Introduction to Finite Element Method (FEM).....	13
2.2.1 FEM Process .....	14
2.2.2 The Mesh .....	15
2.2.3 Principles behind FEM.....	16
2.2.3.1 Variational Principle .....	16
2.2.3.2 Principle of Minimum Potential Energy .....	17
2.3 Contact Analysis with FEM.....	18
2.3.1 Geometrical Contact Conditions .....	18
2.3.2 Contact Formulations.....	20
2.3.2.1 Lagrange Multiplier Method.....	20
2.3.2.2 Pure Penalty Method.....	21
2.3.2.3 Augmented Lagrange Method.....	21
2.4 Introduction to Design of Experiments .....	22
2.4.1 Main Effect and Interaction .....	23
2.4.2 Randomization.....	24
2.4.3 Replication.....	24
2.4.4 Blocking.....	24
2.4.5 Degrees of Freedom.....	25
2.4.6 Confounding .....	25
2.4.7 Full Factorial Design .....	26
<b>3 Experiments .....</b>	<b>27</b>

3.1	The Pressure Measurement Film.....	27
3.2	Experimental Setup .....	28
3.3	Results .....	30
<b>4</b>	<b>Modelling and Simulation.....</b>	<b>32</b>
4.1	Physical Model .....	32
4.2	Mathematical Model .....	34
4.3	Finite Element Model.....	36
4.3.1	The Axle .....	36
4.3.2	The Wheel .....	39
4.3.2.1	Main Wheel Sub-domain.....	40
4.3.2.2	Wheel Sub-domain 2.....	42
4.3.2.3	Wheel-contact Surrounding Area .....	43
4.3.2.4	Wheel Contact Element .....	45
4.3.3	The Rail .....	47
4.3.3.1	Main Rail Sub-domain.....	47
4.3.3.2	Rail-contact Surrounding Area .....	50
4.3.3.3	Rail Contact Element .....	52
4.3.4	Simulation Settings.....	53
4.3.5	DOE Setup .....	54
<b>5</b>	<b>Results and Discussion.....</b>	<b>55</b>
<b>6</b>	<b>Summary .....</b>	<b>64</b>
	<b>Bibliography.....</b>	<b>65</b>
	<b>List of figures.....</b>	<b>67</b>
	<b>List of tables.....</b>	<b>69</b>

## List of abbreviations

Abbreviation	Description
CAD	Computer Aided Design
CAE	Computer Aided Engineering
CPRESS	Contact Pressure distribution
CSTATUS	Contact Status
DOE	Design of Experiments
DOF	Degree of Freedom
FE	Finite Element
FEM	Finite Element Method
HHS	Super High-Pressure Mono-sheet Pressure Measurement Film
HS	High Pressure Mono-sheet Pressure Measurement Film
MS	Medium Pressure Mono-sheet Pressure Measurement Film

## List of symbols

Symbol	Description	Unit
$a, b$	Extents of contact patch	[mm]
$E$	Young's modulus	[MPa]
$E_{A,B(+1)}$	Effect of factor A at 'high' level of factor B	[-]
$E_{A,B(-1)}$	Effect of factor A at 'low' level of factor B	[-]
$f$	Vector of volumetric load	[N mm <sup>-3</sup> ]
$g_N$	Distance function in normal direction	[mm]
$g_T$	Distance function in tangential direction	[mm]
$I_{A,B}$	Interaction between factors A and B	[-]
$K$	Global stiffness matrix	[N mm <sup>-1</sup> ]
$K_e$	Element stiffness matrix	[N mm <sup>-1</sup> ]
$P$	Normal force	[N]
$P_e$	Total potential energy	[J]
$p$	Contact pressure	[MPa]
$p_o$	Maximum contact pressure	[MPa]
$Q$	Tangential force	[N]
$R_e$	Equivalent radius	[mm]
$R', R''$	Principle radii of curvatures at origin	[mm]
$t$	Traction vector	[MPa]
$U$	Strain energy	[J]
$u_1, u_2$	Displacements of surface points S1 and S2 respectively	[mm]
$u_x$	Lateral distance between wheel and rail along x-axis	[mm]
$u_i, v_i, w_i$	Nodal displacements along x, y and z axes respectively	[mm]
$V$	Volume	[mm <sup>3</sup> ]



$W$	Total work	[J]
$X^\nu$	Initial configuration of body $\nu$	[-]
$x^\nu$	Final configuration of body $\nu$	[-]
$\delta_1, \delta_2$	Displacements of bodies at distant points T1 and T2	[mm]
$\varepsilon$	Strain	[-]
$\epsilon_N$	Penalty parameter in normal direction	[-]
$\epsilon_T$	Penalty parameter in tangential direction	[-]
$\eta$	Test function	[-]
$\lambda$	Lagrange multiplier	[N]
$\mu$	Coefficient of friction	[-]
$\nu$	Poisson's ratio	[-]
$\rho$	Strain energy density	[J mm <sup>-3</sup> ]
$\sigma$	Principle stress	[MPa]
$\tau$	Kirchhoff's stress tensor	[MPa]
$\phi_z$	Inclination between tape circle plane and rail center plane in xy-plane	[°]
$\varphi$	Deformation tensor	[mm]
$\Gamma_c^\nu$	Contact surface of body $\nu$	[-]

# 1 Introduction

One of the most important aspect of designing any vehicle is to understand and predict its behavior when it operates. This applies to rail vehicles as well. Any major instability in the dynamics of a rail vehicle would probably arise due to perturbations in wheel-rail interaction. For this purpose, it is critical to study the forces that act between rail and wheel. To comprehend the wheel-rail interaction and the forces they exchange, simplification of the problem is necessary. The first breakthrough in the field of wheel-rail contact occurred when Hertz devised his theory on elastic contacts in 1881 [1]. Since then various theories on wheel-rail contact started emerging. Foundations to modern analysis in general elastic contact mechanics and elastoplastic rolling contact mechanics were laid by J. J. Kalker [2] and K. L. Johnson [3] respectively.

According to de Pater, wheel-rail contact problem can be resolved into Geometric, Kinematic, Tangential and Normal sub-problems [4]. The geometric problem aims to find the points of contact between given rail and wheel profiles by calculating geometrical parameters like local curvature of the profiles. The kinematic problem aims to determine the relative motion between the wheel and rail. The tangential problem calculates the tangential forces that are generated due to friction and creepages in contact area. The normal problem deals with evaluation of the shape and dimensions of contact area and the pressure distribution within the contact patch. For many years, research has been going on the determination of shape and size of wheel-rail contact. Some of the early researches have been purely experimental (e.g. Andrews [5], Poole [6], Pau et al. [7]) or purely simulation based (e.g. Knothe and Le The [8], Telliskivi and Olofsson [9], Piotrowski and Kik [10]). Since they used different wheel-rail contact situation, they could not be compared. Dörner et al. [11] validated Finite Element simulations for wheel-rail normal contact through experiments. The aim of this study is to contribute to the validation of Finite Element calculations of wheel-rail normal contact through DOE and experiments.

The objective of this thesis is to determine the shape and dimensions of contact patch that develop between a stationary wheel and rail and its corresponding pressure distribution using Finite Element Method (FEM). Previous studies show that wheel-rail contact is sensitive to input parameters. Thus, an empirical validation of the simulation is crucial. The experiments are done using a bogie on track. In the experiments, a pressure measurement film (HHS type) is placed between a wheel of the bogie and rail to obtain the contact patch. The experiments are repeated for various positions of wheel and rail. The films are scanned and then post-processed using a special software. The extents of the contact patches are measured using the software itself. For the FE modelling, the 3D models of the wheel and rail are divided into inconsistent sub-regions. The sub-regions are meshed with different element types and sizes. The challenge that one would face in FE modelling of this problem would be in the determination of input values, due to its ambiguous nature. For example, the Angle of inclination of the Rail or lateral position of the wheel with respect to rail cannot be measured precisely. So, a tolerance value has to be added to these measured values.

Thus, we have multiple values for a single input. To help us with this problem, we take the help of Design of Experiments (DOE). DOE helps us not only to organize the inputs, but also to understand the effect of changes in inputs on output. It enables us to find out the best combination of input variables at which we get the desired contact patch. Once the contact patches from simulations are obtained, it is compared with the contact patches from experiments.

## 2 Theoretical Basics

### 2.1 The Wheel-Rail Interface

Studying the wheel-rail contact is critical to understand the dynamic behavior of the vehicle and to estimate the lives of the rail and wheel. Today, railway transportation has become available and economical due to the efficiency of the contact between rail and wheel. However, they still suffer some undesired phenomena like material yielding, stresses, fatigue induced cracks, wear etc. due to various forces like friction, rolling contact forces, lateral and longitudinal forces etc. These phenomena cause undesirable effects like vibration, noise, discomfort to passengers and in worse cases even derailment of the vehicle. A typical Wheel-rail interface is shown in Fig. 1.

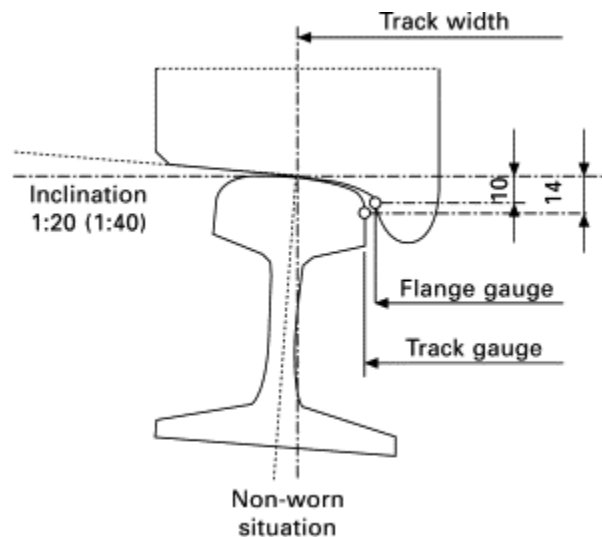
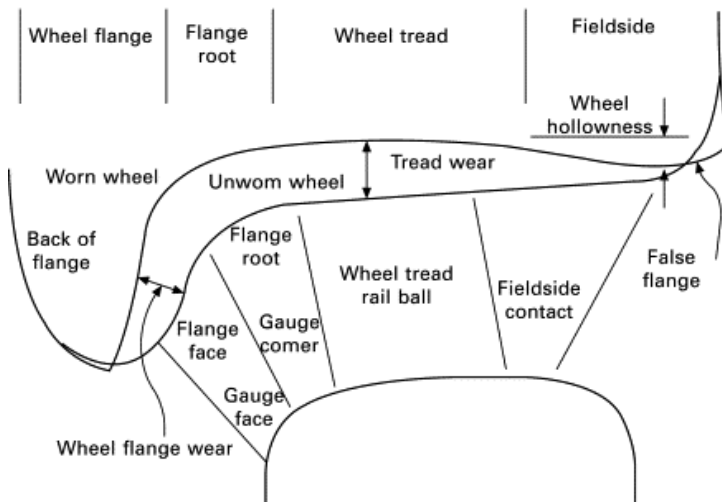


Fig. 1: Wheel profile in contact with rail [1]

#### 2.1.1 Geometry

The profiles of the wheel and rail decide the type, shape and the position of contact patch. The profile of the wheel can be divided into four different regions; Wheel flange, Flange foot, Wheel tread and the Field side. The wheel flange and the flange foot form the inner side of the wheel, the field side, as the name suggests forms the outer side of the wheel and the wheel tread is the middle part of the wheel profile. Similarly, the rail profile can also be divided into four regions; Gauge face, Gauge corner, Rail ball and the Field side. The Gauge face of the rail and the Flange face of the wheel form a contact pair. Similarly, gauge corner - flange foot, rail ball - wheel tread and fieldside contacts form the other contact pairs of wheel-rail interaction. Different regions of the wheel and rail profiles are shown in Fig. 2.



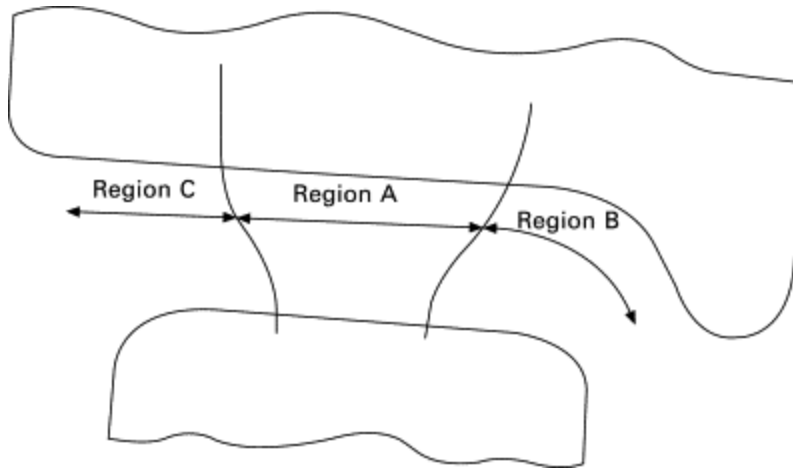
**Fig. 2: Different regions of wheel and rail profiles and wheel in new and worn States [1]**

The wheel profile undergoes tread wear and wheel flange wear as shown in Fig. 2. The tread wear causes skewness in the wheel tread area of the wheel profile. It bends the profile inward, creating a hollowness in the circumference of the wheel. This also creates an undesired false flange in the outer part of wheel profile. The flange wear causes the radius on the flange face to wear out causing a sharp edge on the wheel flange. This is due to constant rubbing of the wheel flange on the rail gauge face. Consequently, the gauge face of the rail also gets worn out. As seen in the figure, the wheel profile is not straight but conical. The conical shape of the wheel profile contributes to the stability of the wheel set and maneuverability of the rail vehicle. The rail is usually inclined inward at an angle between  $1.5^\circ$  and  $3^\circ$  depending upon the standards followed by the country [1].

### 2.1.2 Contact Mechanics

Contact mechanics helps us to understand the effects of two solid bodies coming into contact. It is very critical in understanding the dynamics of a product. Based on the alignment of bodies with each other, contact can be distinguished into two types; Conforming contact and Non-conforming contact. In a conforming contact, one body is conformed exactly by the other body. In other words, the two bodies fit each other exactly due to similar profiles. Journal-bearing is a perfect example for this type of contact. A non-conforming contact, as the name suggests, is opposite to conforming contact. Here, the bodies do not fit each other due to dissimilar profiles. In undeformed state, this type of contact would lead to point or line contact. Rail-wheel contact is an example of non-conforming contact. The type of contact that would emerge between two non-conforming bodies depends on its conformity in different directions. For example, a line contact would appear if the profiles are conforming in one direction and non-conforming in the other direction and a point contact would arise due to non-conformity in all directions. The position of the contact patch that develop between a

wheel and rail varies as the wheel progresses on the track. The position of the patch depends upon the profiles of the wheel and rail, degree of curvature of the track and the position of the wheel in the bogie (i.e. whether it belongs to the leading or trailing wheel set) [1]. The profiles of the rail and wheel can be divided into regions and can be paired. The contact occurs only at the intersection of these contact pairs. The possible regions of contact are shown in Fig. 3.



**Fig. 3: Wheel-rail contact zones [1]**

The Region A is the contact between the wheel tread and the rail head. This is the most common region of contact when the vehicle runs on a straight track. It is also the largest contact region. But the wear in this region is low compared to wear in the wheel flange. Also, the contact stresses are lower in this region. Region B is where the wheel flange and the rail gauge corner come into contact. This contact occurs mostly when the vehicle runs in a curved path. Since contact region is very small compared to wheel head-rail tread contact, the contact stresses are higher in this area leading to severe wear. Higher wear rates might lead to two point contacts. Region C shows the contact between field sides of wheel and rail. This contact is undesirable since it would lead to vehicle maneuverability problems. It is however least likely to occur. The size and shape of the contact changes as the profiles of the wheel and rail changes due to wear. These properties of the contact can be numerically calculated using the Hertz's theory. The theory states that when two elastic non-conforming bodies are brought to contact, the contact area would either be a line or a point depending upon the conformities of the geometry in all directions. As a force is applied on them, the contact area diverges symmetrically from its initial shape. In a wheel-rail problem, bodies can be equated to two cylinders, perpendicular to each other, in contact. This theory however becomes invalid in case of flange contacts and is less accurate. Various solvers have been developed for the Hertzian (FASTSIM - kalker,1982) and non-Hertzian contacts (CONTACT-kalker,1990) which have proven to be more accurate than the Hertz theory. The downside of CONTACT solver is that it needs computers and consumes time. There is a good correlation between Finite Element calculations done by Telliskivi and Olofsson (2001) and the Hertz

and CONTACT analyses in wheel tread contact but different results in flange contact. The comparison between FE, CONTACT and Hertz analysis is shown in Fig. 4.

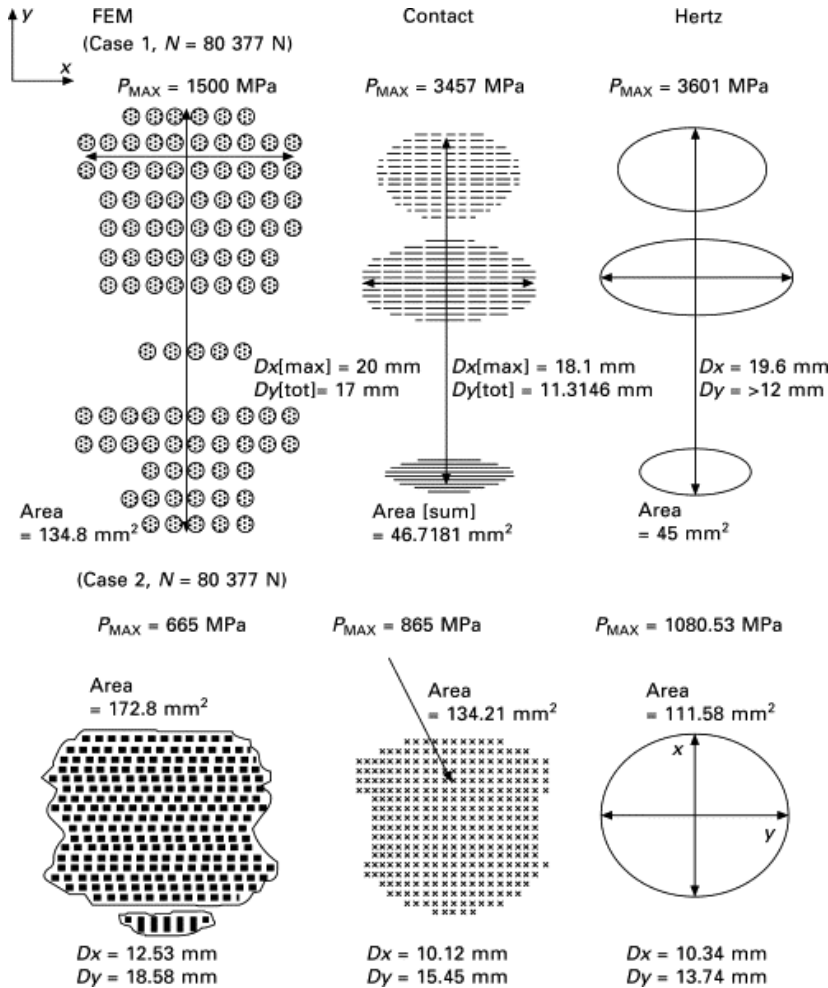
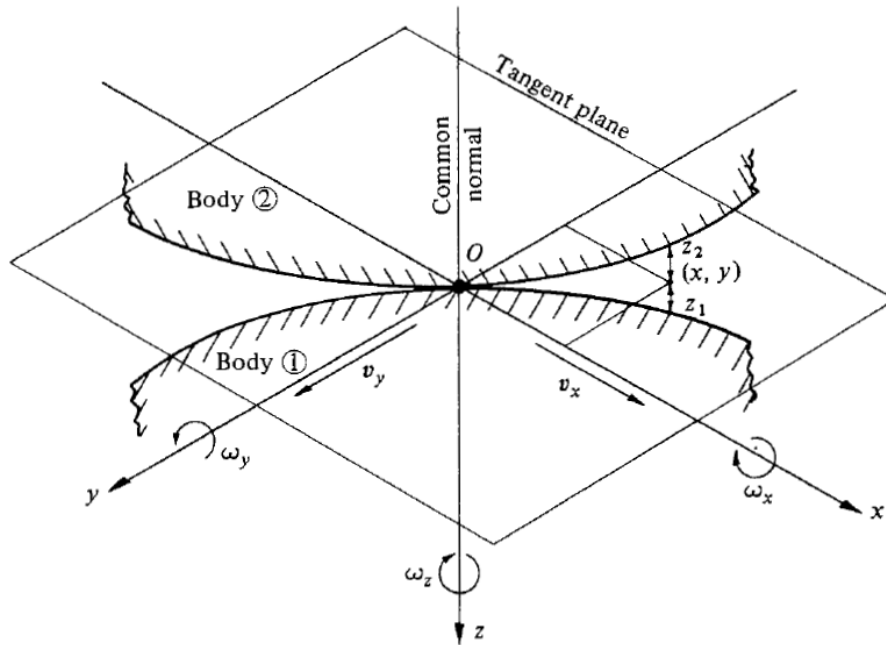


Fig. 4: Comparison between FE, CONTACT and Hertz Analysis [1]

### 2.1.2.1 Frame of Reference

The determination of contact points is crucial in contact mechanics since those are the points at which the forces and moments are exchanged between the bodies in contact. To analytically calculate the points of contact and force transmitted between two non-conforming bodies, we need to define a frame of reference. Let us assume two bodies 1 and 2 in contact at a single point  $O$ . The point  $O$  acts as the origin of a cartesian coordinate with  $O_x$ ,  $O_y$  and  $O_z$  being its axes. The z-axis of the coordinate system coincides with the common normal of both the surfaces of the bodies at  $O$ . The x-y plane is aligned tangent to both the surfaces as shown in Fig. 5.



**Fig. 5: Non-conforming surfaces in Contact [12]**

The profiles of the two surfaces can be defined as a function

$$z_1 = f_1(x, y) \quad (2.1)$$

$$z_2 = f_2(x, y) \quad (2.2)$$

Hence, the separation between these two profiles would be

$$h = z_1 + z_2 \quad (2.3)$$

The forces the bodies transmit at the point of contact can be resolved into Normal force  $P$  acting along the common normal and Tangential force  $Q$  acting along the tangent plane. The normal force is usually compressive in nature and the tangential force is frictional.

$$Q \leq \mu P \quad (2.4)$$

Where  $\mu$  is the friction coefficient. The tangential force  $Q$  is once again resolved into  $Q_x$  and  $Q_y$  acting along  $x$  and  $y$  axis respectively. In a pure Tangential problem, the tangential force reaches its maximum in the direction opposite to the direction of motion. The compressive effect of the Normal force has the capability to deform the solid to create a finite contact area. The pressure distribution inside this area is not uniform. The maximum pressure can be found at the point of contact. The contact pressure pattern depends on the curvature of the bodies at the point of contact.



### 2.1.2.2 Hertz Theory for Elastic Bodies

As discussed earlier, when two non-conforming bodies touch each other, they would have contact at a point or along a line depending upon the conformity of their profiles in different directions. When a force is applied, the bodies deform and a contact area is formed around the point of contact. Hertz formulated a theory to determine the shape of this contact area, various forces and moments that are transmitted at the point of contact and the pressure distribution inside the contact area. The assumptions of the Hertz theory are as follows [12].

1. The surfaces are continuous and non-conforming.
2. The strains are small and the material behavior is linear elastic.
3. The materials are isotropic and homogeneous.
4. Each solid can be considered as an elastic half space.
5. The surfaces are frictionless.
6. The surfaces must be devoid of any irregularities on micro scale and must be continuous (at least quadratic) on macro scale.
7. The surfaces of the bodies are smooth on micro and macro scale.

The theory assumes two bodies touching each other at a single point initially as shown in Fig. 5. Let us describe the profile of the surfaces by

$$z_1 = A_1 x^2 + B_1 y^2 + C_1 xy \quad (2.5)$$

It can also be written as

$$z_1 = \frac{1}{2R_1'} x_1^2 + \frac{1}{2R_1''} y_1^2 \quad (2.6)$$

Where  $R_1'$  and  $R_1''$  are the principal radii of curvature of the surface at origin. They are also the maximum and minimum radius of curvature of all possible cross sections of the profile [12]. Similarly, for second profile

$$z_2 = \frac{1}{2R_2'} x_2^2 + \frac{1}{2R_2''} y_2^2 \quad (2.7)$$

The minimum distance or the separation between the two surfaces is given by

$$h = Ax^2 + By^2 \quad (2.8)$$

or

$$h = Ax^2 + By^2 = \frac{1}{2R'} x^2 + \frac{1}{2R''} y^2 \quad (2.9)$$

Where A and B are positive constants. Assuming the axes  $x_a$  and  $x_b$  to be at an angle of  $\alpha$  to each other,

$$(A+B) = \frac{1}{2} \left( \frac{1}{R'} + \frac{1}{R''} \right) = \frac{1}{2} \left( \frac{1}{R'_1} + \frac{1}{R'_1} + \frac{1}{R'_2} + \frac{1}{R'_2} \right) \quad (2.10)$$

$$|B-A| = \frac{1}{2} \left\{ \left( \frac{1}{R'_1} - \frac{1}{R'_1} \right)^2 + \left( \frac{1}{R'_2} - \frac{1}{R'_2} \right)^2 + 2 \left( \frac{1}{R'_1} - \frac{1}{R'_1} \right) \left( \frac{1}{R'_2} - \frac{1}{R'_2} \right) \cos 2\alpha \right\}^{\frac{1}{2}} \quad (2.11)$$

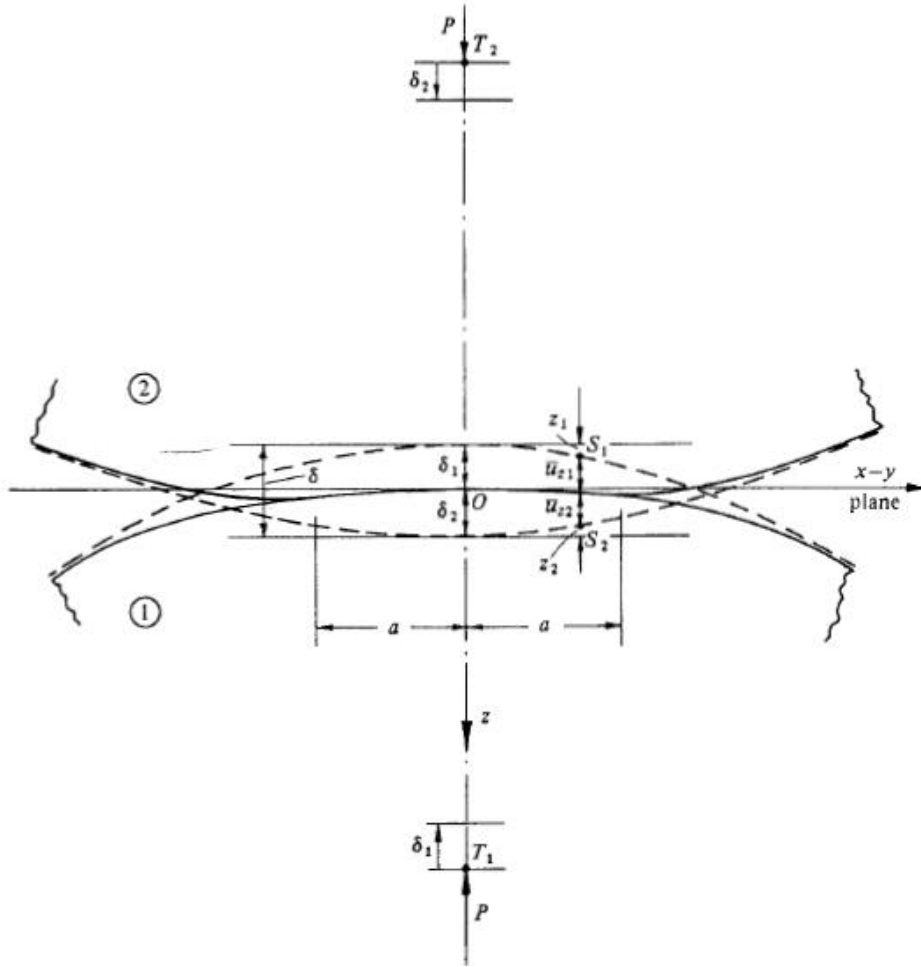
We introduce an equivalent Radius  $R_e$  defined by

$$R_e = (R'R'')^{\frac{1}{2}} = \frac{1}{2} (AB)^{-\frac{1}{2}} \quad (2.12)$$

The surfaces of the two bodies can be convex, concave or saddle shaped. The principle radii would be positive if the surfaces are convex and negative if the surfaces are concave or saddle shaped. From (2.9) it is evident that when the shapes are undeformed, the contact contours would take the shape of an ellipse. The ratio of the lengths of its axes is given by the formula

$$\left( \frac{B}{A} \right)^{\frac{1}{2}} = \left( \frac{R'}{R''} \right)^{\frac{1}{2}} \quad (2.13)$$

If a load  $P$  is applied along the common normal, due to the compressive load, the bodies displace along the  $z$  axis as in Fig. 6. The displacements of the bodies at distant points  $T_1$  and  $T_2$  are given by  $\delta_1$  and  $\delta_2$ . Due to this displacement, the contact area expands symmetrically away from its origin  $O$ . Due to contact pressure, the surfaces are displaced by  $u_1$  and  $u_2$ . If they do not displace, then the surfaces would overlap as shown in Fig. 6.



**Fig. 6: Non-conforming surfaces after deformation [12]**

Thus, after deformation, if the surface points  $S_1$  and  $S_2$  lie within the contact surface, then

$$\overline{u_{z1}} + \overline{u_{z2}} + h = \delta_1 + \delta_2 \quad (2.14)$$

As  $\delta = \delta_1 + \delta_2$ , the elastic displacements are given by,

$$\overline{u_{z1}} + \overline{u_{z2}} = \delta - Ax^2 - By^2 \quad (2.15)$$

If the surface points lie outside the contact region, then

$$\overline{u_{z1}} + \overline{u_{z2}} > \delta - Ax^2 - By^2 \quad (2.16)$$

The pressure distribution at the contact surface needs to be determined and it should satisfy the elastic displacement equations. The pressure distribution is given by the formula

$$p = p_o \left( 1 - \left( \frac{x}{a} \right)^2 - \left( \frac{y}{b} \right)^2 \right)^{\frac{1}{2}} \quad (2.17)$$

Where  $p_o$  is the maximum pressure. The surface displacement within the loaded region due to Hertz pressure is given by

$$\bar{u}_z = \frac{1-\nu^2}{\pi E} (L - Mx^2 - Ny^2) \quad (2.18)$$

This the total displacement is given by,

$$\bar{u}_{z1} + \bar{u}_{z2} = \frac{(L - Mx^2 - Ny^2)}{\pi E^*} \quad (2.19)$$

$$M = \frac{\pi p_o b}{e^2 a^2} \{K(e) - E(e)\} \quad (2.20a)$$

$$N = \frac{\pi p_o b}{e^2 a^2} \left\{ \frac{a^2}{b^2} K(e) - E(e) \right\} \quad (2.20b)$$

$$L = \pi p_o b K(e) \quad (2.20c)$$

Where  $a$  and  $b$  are the semi-major and semi-minor axes of the contact and  $K(e)$  and  $E(e)$  are complete elliptic integrals of the argument

$$e = \left( 1 - \left( \frac{b}{a} \right)^2 \right)^{\frac{1}{2}}, b < a \quad (2.21)$$

The above equation satisfies the condition (2.15), if

$$A = \frac{M}{\pi E^*} = \frac{p_o b}{E^* e^2 a^2} \{K(e) - E(e)\} \quad (2.22a)$$

$$B = \frac{N}{\pi E^*} = \frac{p_o b}{E^* e^2 a^2} \left\{ \frac{a^2}{b^2} K(e) - E(e) \right\} \quad (2.22b)$$

$$\delta = \frac{L}{\pi E^*} = \frac{p_o b}{E^*} K(e) \quad (2.22c)$$

The pressure distribution is ellipsoidal and the total load  $P$  is given by

$$P = \frac{2}{3} p_o \pi ab \quad (2.23)$$

The average pressure is  $p_m = \frac{2}{3} p_o$  (2.24)

or

$$p_o = \frac{3P}{2\pi ab} \quad (2.25)$$

from

The compression  $\delta$  is calculated from (2.22c) and (2.23) as

$$\delta = \left[ \frac{3P}{2\pi ab E^*} \right] b K(e) \quad (2.26)$$

Since  $c = (ab)^{\frac{1}{2}} = \left[ \frac{3PR_e}{4E^*} \right]^{\frac{1}{3}} F_1(e)$ ,  $\delta$  can be re-written as

$$\delta = \left[ \frac{9P^2}{16(E^*)^2 R_e} \right]^{\frac{1}{3}} (F_1(e))^{-1} K(e) \quad (2.27)$$

or

$$\delta = \left[ \frac{9P^2}{16(E^*)^2 R_e} \right]^{\frac{1}{3}} F_2(e) \quad (2.28)$$

Fig. 7 shows the shape of the ellipse ( $b/a$ ) and functions  $F_1$ ,  $F_2$  and  $F_3 (=F_1-2)$  in terms of ratio ( $R'/R''$ ) of relative curvatures for the contact of bodies with general profile.

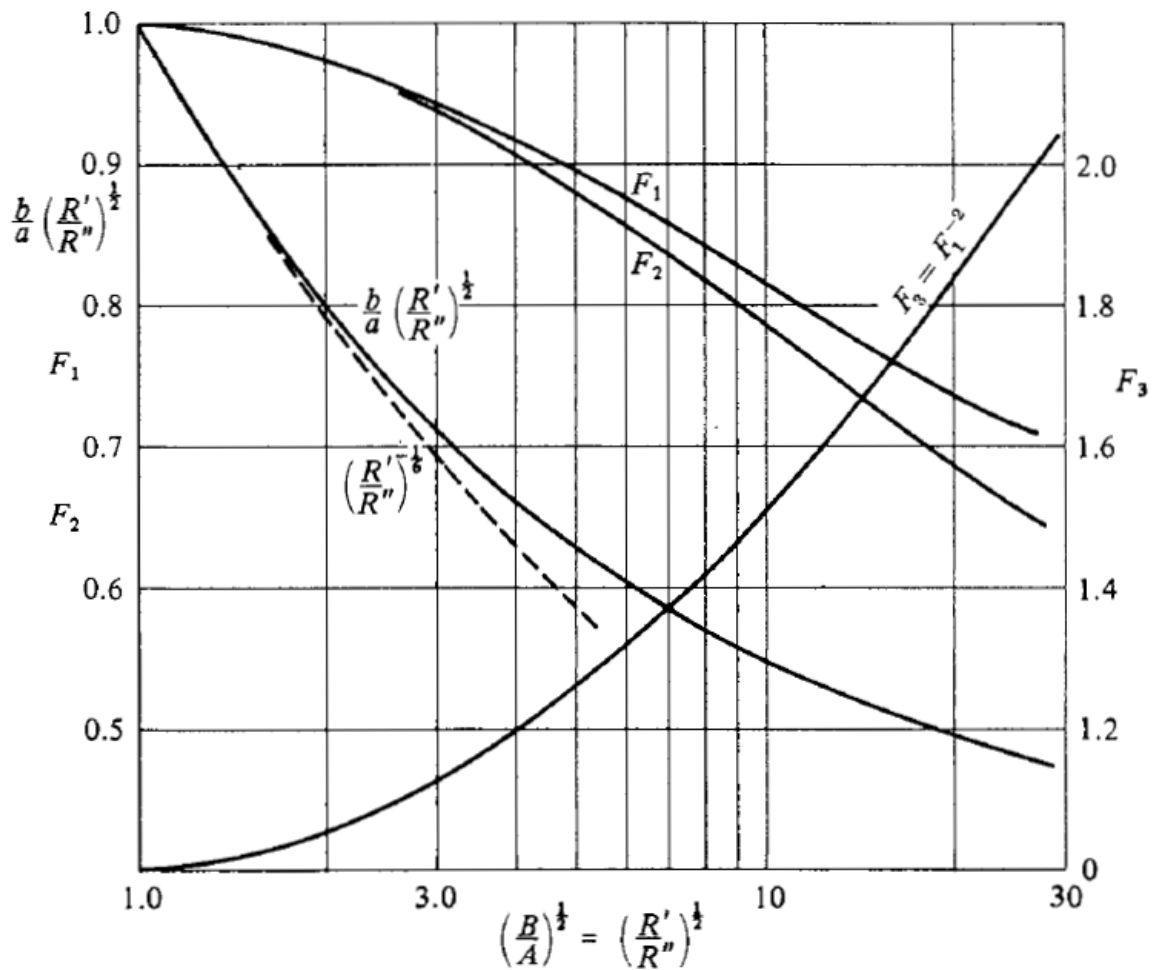


Fig. 7: Contact of bodies with general profile: The shape of the ellipse ( $b/a$ ) and functions  $F_1$ ,  $F_2$  and  $F_3 (=F_1^2)$  in terms of ratio  $(R'/R'')$  of relative curvatures [12]

## 2.2 Introduction to Finite Element Method (FEM)

The Finite Element Method (FEM) or Finite Element Analysis (FEA) is a type of numerical method used for solving a variety of engineering problems. Its areas of application include structural analyses, heat and mass transfer, thermal Analyses, fluid flow, electromagnetics etc. The development of Finite Element Method (FEM) started in mid of twentieth century. The need for the development of FEM rooted from the necessity to calculate and map stresses and strains at various points in working structures. Before the development of FEM, several laws and formulas such as the elastic stress-strain relations, plasticity equations had been developed. The shortcoming of these theories is that, when applying them to structures, basic differential equations had to be solved with complex boundary conditions. This demanded inventive mathematical Analysis to solve even simple problems. This was overcome by converting differential equation to algebraic equation by Ritz [13]. The first attempt to divide the structure in to triangular elements was made by Courant [13]. He used the principle of minimization of potential energy and piecewise polynomial variations to solve

a problem of St Venant variation [13]. The later developments in FEM includes invention of "Matrix Handling Scheme" in computers, Development of Iso-parametric elements, Ability to solve plasticity and creep behavior, Ability to do dynamic calculations etc. The development of Iso-parametric elements was one of the critical developments in the evolution of FEM. Though computers were becoming bigger and powerful, it was difficult to accommodate many triangular elements in analyses. Since the accuracy of hexahedral elements is way better than triangular elements, combining of both type of elements in Analyses proved to be efficient. The development in computers has also contributed to evolution of FEM in a large way. In 1950s, FEM was used only by aerospace, nuclear and large Industries as computers were very unaffordable and limited. Today, with development of personal computers, FEM is made available for everyone. From static, dynamic to thermal and electromagnetics, it can solve a wide range of problems.

### 2.2.1 FEM Process

The FEM process can be divided into three parts; Pre-processing, Solution and Post-processing. The pre-processing involves FE modelling of the problem which includes meshing the structure into elements and nodes, applying boundary condition and loads, assigning material properties etc. Solving step includes finding the solution of the problem by solving the stiffness equation. The solution can be the unknown displacements, stresses and strains at nodes in a structural problem, temperature in a thermal problem etc. The stiffness equation is given by

$$[K]\{u\} = \{F\} \quad (2.29)$$

where  $K$  is the stiffness matrix of the structure,  $u$  is vector of all nodal displacements and  $F$  is vector of all the applied nodal forces. The element stiffness matrix  $[K_e]$  is first calculated for each element and then assembled into a global stiffness matrix  $[K]$ . From the applied loads and calculated stiffness matrix, the nodal displacements are calculated. From the displacements, the stresses and strains are calculated. The obtained results are then stored and post-processed. The process flow chart of FEM is shown in Fig. 8.

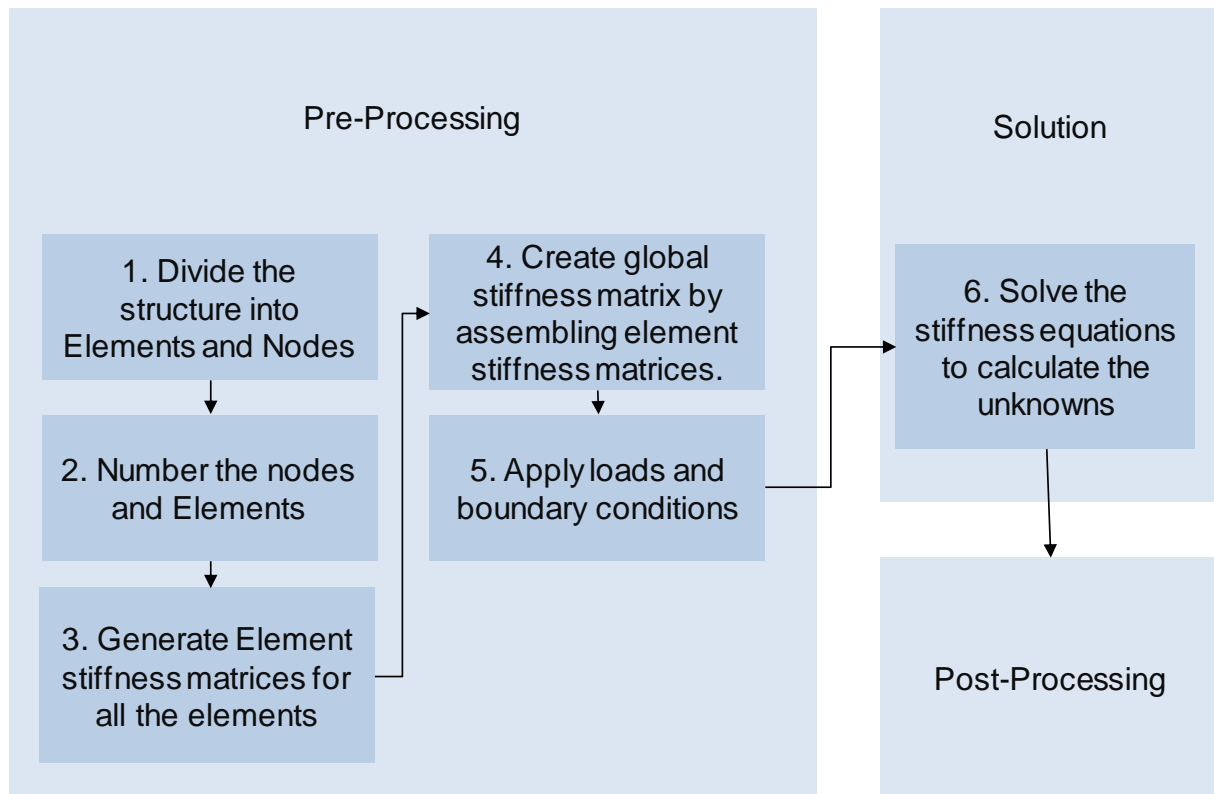


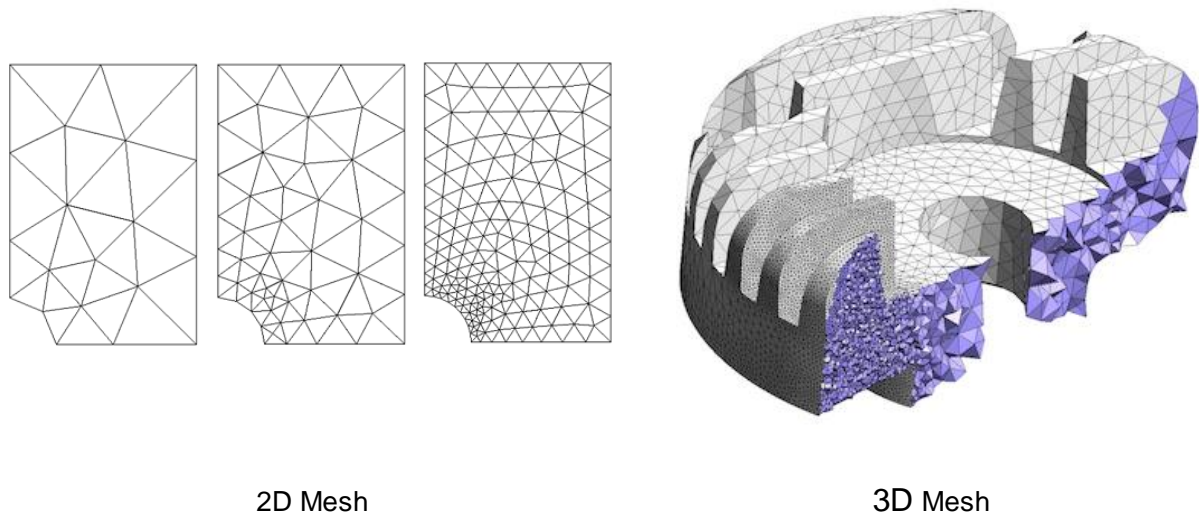
Fig. 8: FEM process flow chart

### 2.2.2 The Mesh

Before applying boundary conditions and load, the structure is divided into elements that are too small compared to its size. Elements can be 1D, 2D or 3D depending upon the type of the structure. For example, for planar structures 2D elements are used and for solid structures 3D elements are used. Every element has a defined number of reference points called nodes. Every node in a structure has a maximum of 6 degree of freedom depending upon the type of element used. They are the translation degrees of freedom and the rotational degrees of freedom. Every node can have displacements in x, y and z directions denoted by  $u_i$ ,  $v_i$  and  $w_i$  and rotations about x, y and z axes denoted by  $\Phi$ ,  $\sigma$  and  $\theta$ . They are also called as Field variables or Primary variables. Another class of variable called Secondary variables include stress, strain and heat fluxes. They are derived from primary variables. The displacements are calculated at the element nodes but the stresses are calculated at the integration points and extrapolated to the nodes. Elements can be of different shapes and order. The number of nodes in an element depends upon the shape and order of element. For example, a 2D element can take the shape of a triangle or a quadrilateral. First and second order triangular element have three and six nodes respectively and quadrilateral elements have four nodes and eight nodes respectively. First order elements usually have nodes at their corners and higher order elements have their nodes at their corners as well as at the sides, depending upon their order. Similarly, 3D



elements can take the shape of a Hexahedron or a Tetrahedron and can be of different orders. A typical example of a 2D and 3D mesh are shown in Fig. 9. The type and number of elements in a model affects the accuracy of the solution. The accuracy of the solution increases as the number of elements in a model increases. However, the solution time increases as the number of elements are increased. The optimum number of elements can be known only by trial and error method.



**Fig. 9:** Example of a 2D and 3D FE mesh [14] [15]

## 2.2.3 Principles behind FEM

### 2.2.3.1 Variational Principle

Principle of minimum potential energy forms the basis of Finite Element Method. To understand this principle, it is crucial to understand the variational principle. To solve a problem numerically, a set of information like the geometry, material properties, boundary conditions, loads etc. is necessary to analyze and determine the new state of the system. The initial physical state can be numerically represented by partial differential equations and boundary conditions. When these partial differential equations are defined as an integral equation, the resultant expression is called as a functional. Functional is a generic term. In FEM, the most commonly used functional is the total potential energy. It represents the total potential energy of a system and usually contains the equation of the system integrated over the volume. Variational principle solves these partial differential equations by finding the conditions at which the functional is stationary. In stress analysis, stationary value of the functional (i.e. total potential energy) would imply the points at which the total potential energy of the system will be minimum [13]. Variational Principle also has other names like variational method, variational approach and energy method.

### 2.2.3.2 Principle of Minimum Potential Energy

For a body to deform from its original state, it needs energy. This energy is obtained from the loads applied and it is called strain energy  $U$ . It is a function of stresses and strains and is distributed throughout the volume of the body. It is obtained by integrating the strain energy density  $p$  over the whole volume  $V$ .

$$U = \frac{1}{2} \int_V \{\sigma\}^T \{\varepsilon\} dV \quad (2.30)$$

Let us assume a body that has undergone a nodal displacement  $u_i$  due to applied force  $F_i$ . The external force also comprises of internal forces like the gravity, centrifugal force etc. Thus, the work done by the external force would be

$$W = \sum_i \{F_i\}^T \{u_i\} \quad (2.31)$$

The work done is over all degrees of freedom and all the nodes in the structure. The value of  $F_i$  would be zero if there are no external forces applied on that node. Now, the total potential energy  $P_e$  of the body is the difference between Strain energy  $U$  that got induced in the body due to applied force and the work done by the external forces  $W$  on the body

$$P_e = U - W \quad (2.32)$$

When a displacement of  $u_i$  is applied on a body in equilibrium, the work done due to the Forces  $F_i$  induced due to applied displacements should be equal to the strain energy developed inside the body to attain equilibrium again.

$$dU = d(\{F_i\}^T \{u_i\}) \quad (2.33)$$

$$d(U - \{F_i\}^T \{u_i\}) = 0 \quad (2.34)$$

$$dP_e = 0 \quad (2.35)$$

The principle of minimum potential energy states that, among any combination of admissible displacements, those which give the correct solution produce minimum value of potential energy [13]. This principle is also called as Hu-Washizu principle. In mathematical sense, for a body to be in external and internal equilibrium, the function  $P$  should be stationary in all degrees of freedom. The function  $P$  can be minimum or maximum. If  $P$  is minimum, the equilibrium is stable and vice versa. The equilibrium condition is

$$\frac{\partial P_e}{\partial u_i} = 0 \quad (2.36)$$

## 2.3 Contact Analysis with FEM

A contact is considered as a non-linearity in FEM since they cause changes to the boundary conditions of the system when the status of the contact changes from open to close and vice versa. Physically, when two bodies touch each other, they do not interpenetrate. They transmit compressive forces (both normally and tangentially). To understand how a software recognizes bodies in contact and how the contact forces calculated, it is necessary to understand the contact formulations.

### 2.3.1 Geometrical Contact Conditions

Following [16], the numerical contact condition of two bodies can be understood. Let us consider two convex bodies  $B^1$  and  $B^2$  as shown in Fig. 10. Both the bodies can be represented by  $B^\gamma$ ;  $\gamma = 1, 2$ . The initial configuration and the deformed configuration of the bodies are given by  $X^\gamma$  and  $x^\gamma$  respectively ( $X \in B^\gamma$ ). The deformation  $\varphi^\gamma$  converts the body from its initial configuration to its final configuration. A contact surface on these bodies is represented by  $\Gamma_c^\gamma \subset \partial B^\gamma$ . The two surfaces on these bodies are assumed to be convex.

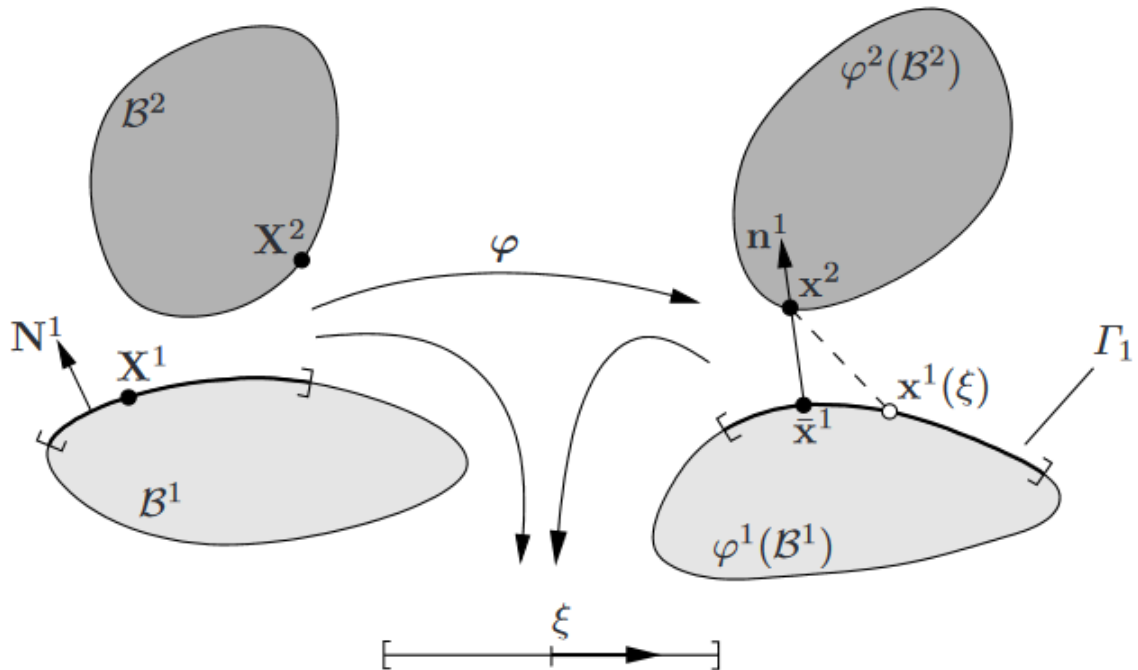


Fig. 10: Contact geometry and geometric approach [16]

To formulate the distance and the penetration function mathematically, it is required to distinguish the surfaces. Thus, the bodies 1 and 2 are named as the slave and master respectively. It can also be vice versa. The deformations of these surfaces are represented by  $\varphi^1(\Gamma_c^1)$  and  $\varphi^2(\Gamma_c^2)$  respectively. Now, the master surface  $\Gamma_c^2$  is parametrized in all its

configurations by convective coordinates. Thus, in initial and current configurations, the material surfaces are described by  $X^2 = \hat{X}^2(\xi^1, \xi^2)$  and  $x^2 = \hat{x}^2(\xi^1, \xi^2)$  respectively. The tangent vectors are given by  $A_\alpha^2 = \hat{X}_{,\alpha}^2(\xi^1, \xi^2)$  and  $a_\alpha^2 = \hat{x}_{,\alpha}^2(\xi^1, \xi^2)$  respectively. Now let us select a point  $\bar{x}^2$  on body 2 such that, it is the closest to the point  $x^1$  on body 1. It is determined from

$$\|X^1 - \bar{X}^2\| = \min_{x^2 \in \Gamma^2} \|x^1 - x^2(\xi)\| \quad (2.37)$$

and

$$\frac{d}{d\xi^\alpha} \|x^1 - x^2(\xi^1, \xi^2)\| = \frac{x^1 - x^2(\xi^1, \xi^2)}{\|x^1 - x^2(\xi^1, \xi^2)\|} \cdot x_{,\alpha}^2(\xi^1, \xi^2) = 0 \quad (2.38)$$

Once  $\bar{x}^2$  is known, an inequality condition describing the non-penetration of the solids can be defined. The distance function is given by

$$g_N = [x^1 - x^2(\bar{\xi})] \cdot n^2(\bar{\xi}) \quad (2.39)$$

And the constraint condition is given by

$$g_N = [x^1 - \bar{x}^2] \cdot \bar{n}^2 \geq 0 \quad (2.40)$$

if

$g_N > 0$ , The bodies are not in contact

$g_N = 0$ , The bodies are in contact

$g_N < 0$ , The bodies are interpenetrating

The penetration function is given by,

$$\bar{g}_N = (x^1 - \bar{x}^2) \cdot \bar{n}^2 \text{ if } (x^1 - \bar{x}^2) \cdot \bar{n}^2 < 0 \quad (2.41)$$

else,

$$\bar{g}_N = 0 \quad (2.42)$$

### 2.3.2 Contact Formulations

The three well known contact formulations are the pure penalty method, the augmented lagrange Method and the pure lagrange method. The Pure penalty and the augmented lagrange method are called penalty based methods. These methods introduce a contact element (a contact spring) at the point of contact. By this, the contact force is resolved into stiffness and penetration. The penetration is the extent to which the bodies interpenetrate each other. The stiffness ratio of the element is defined by the user and it determines the penetration. Low value of stiffness leads to higher penetration and subsequently inaccurate results. A higher value of stiffness would lead to zero penetration and difficulty in convergence (due to chattering) subsequently. The stiffness is usually defined as a factor. The difference between the pure penalty and the augmented lagrange method is that the latter adds another term (the multiplier  $\lambda$ ) to the equation. This makes the method less sensitive to contact stiffness. The method provides better accuracy of results compared to the pure penalty method. The lagrange multiplier method is a direct method in which the contact pressure is not resolved into stiffness and penetration but solved as additional degree of freedom. Also, in this method the interpenetration of the bodies is zero. The inequality equation representing the contact condition leads to variational inequality of the form

$$\sum_{\gamma=1}^2 \int_{\Omega^\gamma} \tau^\gamma \cdot \nabla^S (\eta^\gamma - \phi^\gamma) dV \geq \sum_{\gamma=1}^2 \int_{\Omega^\gamma} \bar{f}^\gamma \cdot (\eta^\gamma - \phi^\gamma) dV - \int_{\Gamma\sigma^\gamma} \bar{t}^\gamma \cdot (\eta^\gamma - \phi^\gamma) dA \quad (2.43)$$

When the pure penalty and lagrange formulations are used in FEM, the inequality constraints are divided into active and inactive constraints changing their number within the solution [16]. A variational equation instead of variational inequality can be formulated in contact area as

$$\sum_{\gamma=1}^2 \left\{ \int_{\Omega^\gamma} \bar{\tau}^\gamma \cdot \text{grad} \eta^\gamma dV - \int_{\Omega^\gamma} \bar{f}^\gamma \cdot \eta^\gamma dV - \int_{\Gamma\sigma^\gamma} \bar{t}^\gamma \cdot \eta^\gamma dA \right\} + \text{"contact contributions"} = 0 \quad (2.44)$$

The contact contributions in the above equation can now be formulated with the above-mentioned methods

#### 2.3.2.1 Lagrange Multiplier Method

The contact contribution for lagrange multiplier method is

$$\int_{\Gamma_C^{akt}} (\lambda_N \delta g_N + \lambda_T \cdot \delta g_T) dA \quad (2.45)$$

Where,  $\lambda_N$  is the lagrange multiplier, which in contact problems can be identified as contact pressure ( $p_N$ ),  $\delta g_N$  is the variation of distance function in the normal direction and  $\lambda_T \cdot \delta g_T$  is the constraint in tangential direction.

### 2.3.2.2 Pure Penalty Method

In pure penalty method, the contact constraint  $g_N = 0$  is introduced in the weak form using a penalty term. Thus,

$$\int_{\Gamma_C} (\epsilon_N \lambda_N \delta g_N) dA, \quad \epsilon_N > 0 \quad (2.46)$$

If  $\epsilon_N \rightarrow \infty$ , then the result of lagrange multiplier is recovered [16]. However, a large penalty parameter would lead to badly conditioned tangential stiffness matrix. The slip and stick in the tangential direction must be distinguished. Thus, for stick,

$$\int_{\Gamma_C} (\epsilon_N \lambda_N \delta g_N + \epsilon_T g_T \cdot \delta g_T) dA, \quad \epsilon_N > 0, \quad \epsilon_T > 0 \quad (2.47)$$

and for slip,

$$\int_{\Gamma_C} (\epsilon_N \lambda_N \delta g_N + t_T \cdot \delta g_T) dA, \quad \epsilon > 0 \quad (2.48)$$

### 2.3.2.3 Augmented Lagrange Method

The issue with penalty method as discussed above is the ill conditioned tangent stiffness matrix when penalty parameter is large. The augmented lagrange method solves this problem. This method is based on the UZAWA-algorithm. It is based on the idea to fix the lagrange multiplier within an iterative solution step and then compute the next value of the lagrange multiplier by an update formula [16]. The weak form of this method is

$$\sum_{\gamma=1}^2 \left\{ \int_{\Omega^\gamma} \bar{\tau}^\gamma \cdot \text{grad} \eta^\gamma dV - \int_{\Omega^\gamma} \bar{f}^\gamma \cdot \eta^\gamma dV - \int_{\Gamma_{\sigma^\gamma}} \bar{t}^\gamma \cdot \eta^\gamma dA \right\} + \int_{\Gamma_C} [(\bar{\lambda}_N + \epsilon_N g_N^L) \delta g_N + t_T \cdot \delta g_T] dA = 0 \quad (2.49)$$

With an update

$$\bar{\lambda}_{N_{new}} = \bar{\lambda}_{N_{old}} + \epsilon_N g_{N_{new}} \quad (2.50)$$

## 2.4 Introduction to Design of Experiments

An experiment is an act or an operation for discovering an unknown. In an engineering, experiments are conducted to explore, estimate or confirm. Estimation is nothing but the determination of the effects of process variables or factors on output. Estimation is necessary to optimize any system or process to produce desired results. It helps us understand how the changes in input variables affect the output. For example, in a turning operation, the speed of the chuck, the feed rate, coolant flow rate etc. determine the surface finish. Here the chuck's speed, feed rate and the coolant flow rate are the influencing factors and the surface finish is the output. By varying these input values, their effect on surface finish can be found out. The process can be optimized by determining the best combination of inputs for which we get the desired surface finish. One of the most common method used in manufacturing industries is OVAT. OVAT is an abbreviation of One Variable At a Time. The idea behind this method is to determine the effect of inputs by varying the value of one input and keeping the other inputs unchanged. This method needs large resources to carry out the experiments and the information obtained is however limited. Also, the success of this method depends on the experience of the person carrying out the experiments, luck and intuition. Other way of carrying out this analysis is through statistical method called Design of Experiments (DOE).

DOE is a process of designing and analyzing an experiment to draw conclusions and inferences from its outcome. In a designed experiment, variations of the input variables are made deliberately to study its effect on the output. It is indeed the best tool to choose when a bountiful amount of inputs influences the output variable. DOE was invented by Sir Donald Fisher in 1920s at Rothamsted Agricultural Field Research Station in London, England [17]. He used DOE for determining the effect of various fertilizers on crop yield. Since other factors like soil condition, moisture content etc. also decide the crop yield, he differentiated the effect of fertilizers alone on crop yield through design of experiments. The input variables of an experiment are called factors.

Factors are of two types; Qualitative and Quantitative factors. Qualitative factors refer to those that can be differentiated by their type. For example, type of supplier, type of catalyst, type of raw material etc. are qualitative factors. They are discrete in nature. Quantitative factors are those that can be quantified, like temperature, speed, flow rate etc. In DOE, every factor is given a certain number of values called levels. For example, if five different types of catalysts are selected for an experiment, then the number of levels for the raw material factor is five and if three different temperature settings are selected, then the number of levels for temperature factor is three. Usually, qualitative factors have more number of levels than the quantitative factors. The three principles of DOE are the Randomization, Replication and Blocking. These principles can be used to improve the experimentation efficiency

### 2.4.1 Main Effect and Interaction

Main effect in design of experiments is the effect of a single factor on the response averaged across all the levels of other factors of an experiment. Interaction refers to the combined effect of two (or more) factors on the response of an experiment. Two variables of an experiment interact if the effect of one of the variables changes depending upon the levels of the other variable. Let us consider two factors A and B. Each factor is assigned with two levels (+1 and -1) as shown in Fig. 11. The main effect of factor A on response is calculated as follows. First the average value of the responses of both the levels of factor A at all the levels (+1 and -1) of factor B is determined. A line connecting these two values would give the main effect of factor A. It is represented by blue line in Fig. 11. Main effect of Factor B can be determined by same method. Interaction is represented by red lines. In this case, non-parallel lines imply that, as the levels of factor B changes, the response due to factor A also changes. This means that the factors are interacting. If the lines are parallel, then one can say that the factors are not interacting. Interaction between two factors with two levels is given by the formula

$$I_{A,B} = \frac{1}{2} (E_{A,B(+1)} - E_{A,B(-1)}) \quad (2.51)$$

Where  $I_{A,B}$  is the interaction between factors A and B,  $E_{A,B(+1)}$  is the effect of A at 'high' level of B and  $E_{A,B(-1)}$  is the effect of A on 'low' level of factor B.

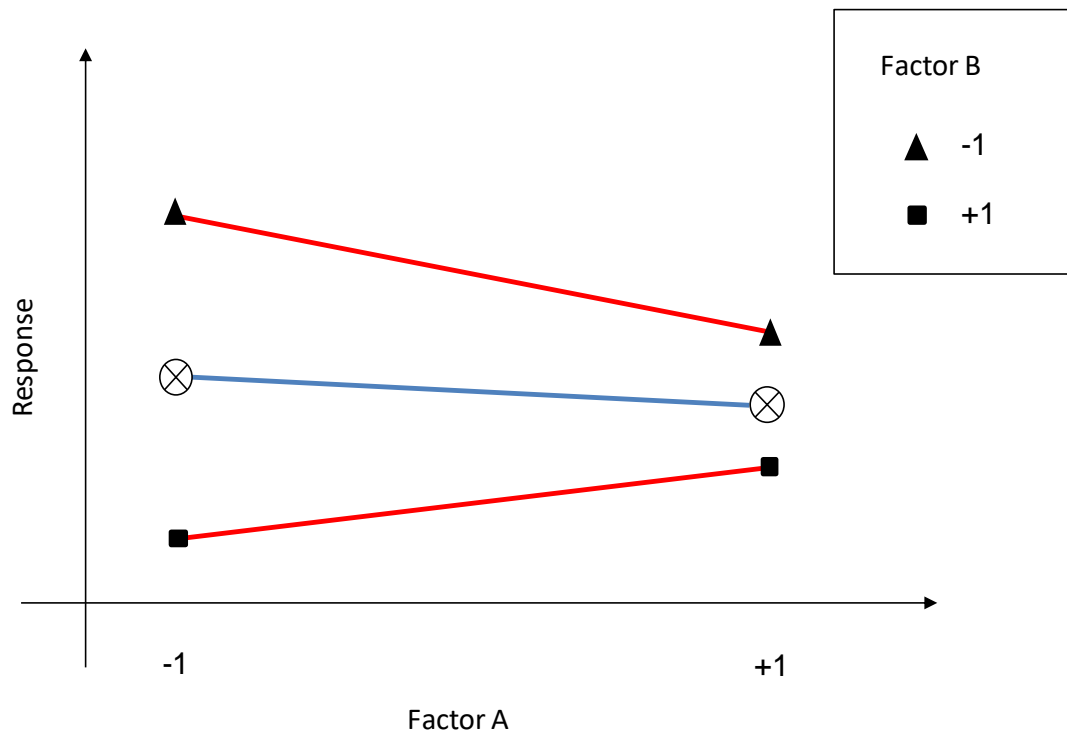


Fig. 11: Main effects and Interactions



## 2.4.2 Randomization

Randomization is a process of randomly recording the outcomes of an experiment to remove all sources of uncontrollable extraneous variations. Every process of a system is affected by a noise. For example, a machine cannot be efficient throughout its life. Factors like wear and fatigue affect the performance of the machine. Similarly, the person who operates the machine cannot be efficient all the times. The idea of randomization is to make sure that all the levels of a factor are equally affected by these noise factors. Randomizing an experiment averages out the effects of noise factors present in a system. This can be explained with an example situation. If an experimenter wants to know the effects of chuck speed on surface finish in a lathe and decides to make note of the surface finish values by continuously increasing the speed, the data would show that the surface finish would degrade with increase in speeds. But in actual case the surface finish would be better with increase in speeds. The error occurs due to heating of the tool caused by continuously increasing speeds. This error can be avoided by randomization. Instead of continuously increasing the speed and recording the values, the speed can be randomly varied to avoid tool heating and the corresponding surface finish values can be noted.

## 2.4.3 Replication

Replication is a process of repeating the set of experiments or a part of it under different conditions. However, it is different from repetition. Repetition would mean repeating an experiment several times before getting to another. In replication, all the experiments are done once before repeating the experiments all over again. Repeating experiments several times allows the experimenter to determine the experimental error precisely and to reduce them sufficiently. Experimental errors occur despite using same experimental units (machines, material etc.) and settings. Replication also enables the experimenter to estimate the factor/interaction effects precisely. Higher the number of replicates, better the odds of precise determination of errors and interaction effects. The disadvantage with replication is that, the process is expensive and time consuming.

## 2.4.4 Blocking

Blocking is the grouping of a set of similar, homogenous experiments into blocks. The idea of blocking is to eliminate the effect of noise factors on output by eliminating the variations that occur in the experimental conditions between days, shifts or batches. For example, if two replicates of an experimental set are done on two successive days, the first replicate is named as block 1 and the second replicate is named as block 2. It is made sure that there is no variation in conditions within a block. i.e. the materials used, the operations and other conditions are maintained the same. The variation that would occur between the blocks is the noise factor that is induced due to difference in conditions between day 1 and 2.

### 2.4.5 Degrees of Freedom

Statistical definition of Degrees of Freedom (DOF) is the number of comparisons that can be made in a set of data [17]. It is one less than the number of levels of a factor in an experiment. For example, if the lengths of three rods are compared, then the number of levels of the factor length is 3. Thus, the degrees of freedom for the main effect due to that factor is 2 ( $=3-1$ ). If there are six factors in an experiment with three levels for each factor, then the degrees of freedom for all the main effects is 12 ( $=(3-1) \times 6$ ). Degrees of freedom can also be determined for a complete experiment and for an interaction. For an experiment, the degrees of freedom is one less than the total number of observations. For example, if there are twenty runs in a set of experiment and it is replicated thrice, then the total number of experiments is 60 and the degrees of freedom for the experiments is 59 ( $=60-1$ ). The degrees of freedom for an interaction is the product of degrees of freedom of the factors involved. For example, if there are two factors with three levels, then the degrees of freedom for each factor would be 2. Thus, the degrees of freedom for the interaction would be 4 ( $=2 \times 2$ ). If the number of factors is four, then the DOF for all the six interactions is 24 ( $=(3-1) \times (3-1) \times 6$ ).

### 2.4.6 Confounding

Confounding or aliasing is the combined effect of two or more factors on an measurand. Confounding makes it impossible to estimate the factor effects and interaction effects independently. For example, in studying the effect of coolant flow rate and feed rate on surface finish in a machining process, let us assume that the two factors are assigned with two levels (Low and High). If the levels are set at low/low and high/high and the effect on surface finish is studied as shown in Tab. 1, then the individual effects due to coolant flow rate and the feed rate cannot be studied. This because, the effect of both coolant flow rate and feed rate would be x-y. Thus, one cannot tell if the calculated effect is due to coolant flow rate or feed rate.

**Tab. 1: Example for confounding**

Coolant Flow Rate	Feed rate	Surface finish
Low	Low	x
High	High	y

## 2.4.7 Full Factorial Design

Full factorial and Fractional factorial designs are the most commonly used DOE methods in industries. A factorial design consists of two or more factors with discrete values called levels assigned to them. It allows the experimenter to find out the effect of factors on the response and the effect of interaction between two or more factors on the measurand. The number of combinations or the number of trials in an experiment with full factorial design is given by number of factor times the number of levels assigned for each factor. For example, if there are five process variables and the number of levels assigned for these factors is 2, then the total number of experiments to be carried out is  $32 (=2^5)$ . The most commonly used design when the experiments are at the preliminary stage is  $2^k$  full factorial design. It is also recommended when the number of factors ( $k$ ) is less than or equal to four. The design consists of  $k$  factors with 2 levels assigned to them. The levels are usually represented by +1 and -1. An example of  $2^2$  full factorial design is shown in Tab. 2.

**Tab. 2: Example of  $2^2$  full factorial design**

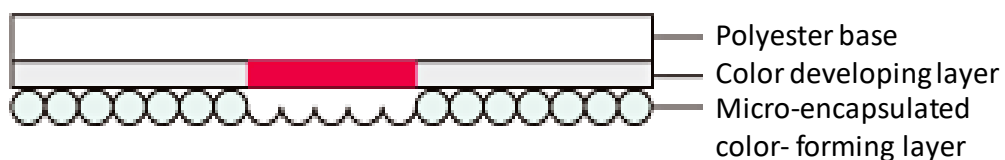
Exp. No.	A	B
1	+1	+1
2	+1	-1
3	-1	+1
4	-1	-1

### 3 Experiments

The purpose of the experiments is to validate the contact patch obtained from the simulations. Only few methods are known for determining the contact patch experimentally. The first method is to obtain the imprint using a carbon paper. This method was developed by Poole [4]. The disadvantage with this method is that, it shows bigger contact area than the actual one. The second method uses ultrasounds to determine the contact area [5]. One can also determine the corresponding pressure distribution within the contact path using this method. The drawback of this method is that, the determination of the boundary is complex process. The third and the best-known method is the determination of contact path using Prescale pressure measurement film. It is similar to carbon paper method, but the systematic error is comparatively low. Though the method suffers minor catches like over-estimation of contact patch, it is found to be the best option available for wheel-rail contact situations.

#### 3.1 The Pressure Measurement Film

The method of determination of contact patch using pressure measurement films is undemanding. The contact patch is first obtained by applying pressure on the film and then the film is scanned by a scanning software for the evaluation of the results. There are different types of pressure measurement films. The one used in this experiment is a mono-sheet pressure measurement film. Three types of mono-sheet pressure measurement films are available; HHS, HS and MS. The pressure range for MS, HS and the HHS are 10 MPa - 50 MPa, 50 MPa – 130 MPa and 130 MPa – 300 MPa respectively. The HHS pressure measurement film is selected for the experiments since they have proven to yield better results and are more suitable for wheel-rail contact problems [18]. The pressure measurement film has a polyester base overlapped by a color developing layer and a micro encapsulated color-forming layer as shown in Fig. 12.

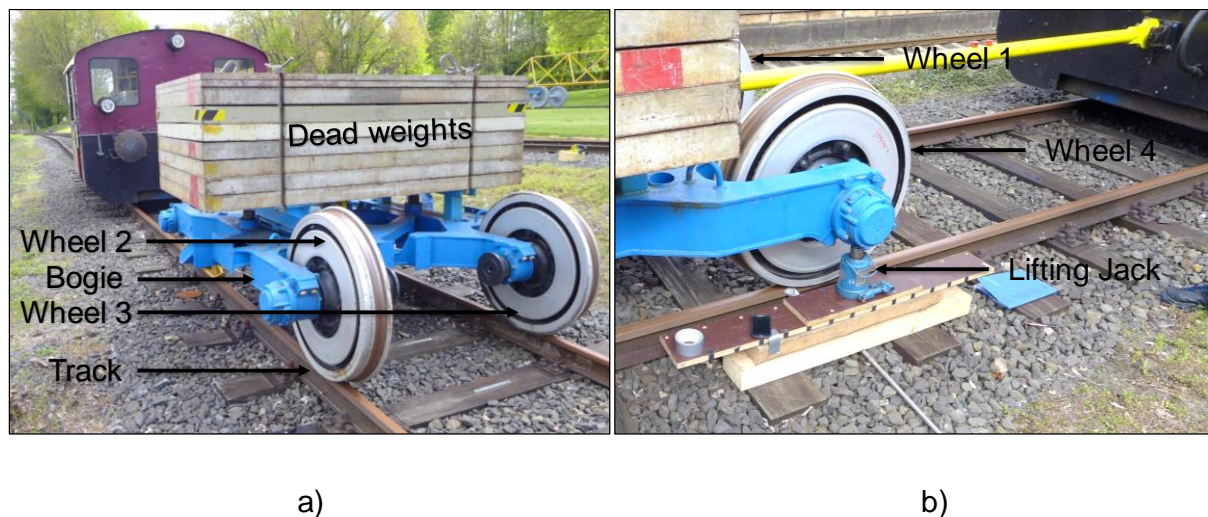


**Fig. 12: Cross-section view of the mono-sheet pressure measurement film [19]**

The color forming layer consists of micro capsules of different sizes. When the pressure applied on the film reaches a limit value, the micro capsules in the micro encapsulated color forming layer burst releasing the fluid they contain. The fluid reacts with the color developing layer forming red blotches of different intensity. The intensity depends on the applied pressure.

### 3.2 Experimental Setup

The experimental setup consists of a four-wheeled railway bogie loaded with deadweights. The purpose of the deadweight is to create optimum pressure to form contact patch similar to real wheel-rail contact. The wheels are numbered for reference and the load acting at individual wheels are measured using an overhead scale at the workshop. The values obtained are in tonnes. The bogie is then attached to a shunting engine and moved to the track where the experiments are done as shown in Fig. 13(a). Since the tracks used for experiments are old, the bogie is first moved back and forth to smoothen its surface. Based on the quality of the wheel, two of them are chosen for experiment. For this experiment, wheels 1 and 4, which form the front wheels of the bogie are selected. The wheels are thoroughly cleaned to remove all the rust and dust that had developed on the surface. The same is done to the rails as well.

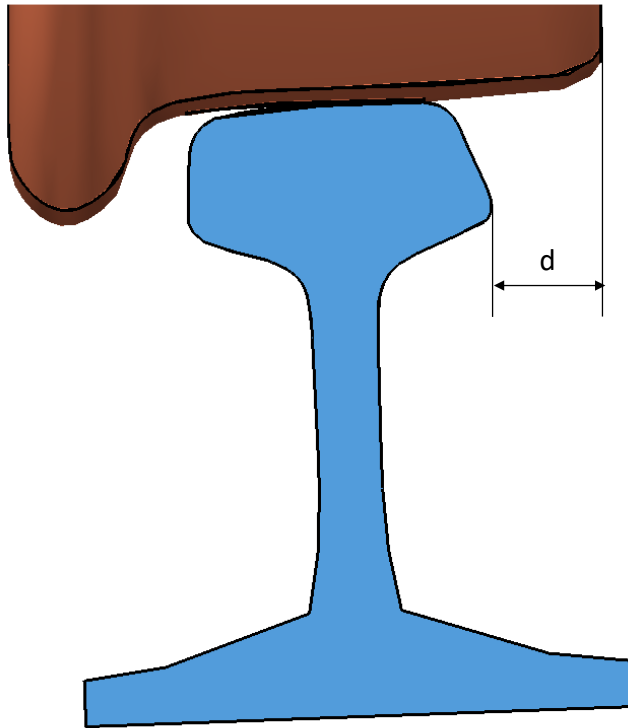


**Fig. 13: Experimental setup**

The experiments are done at four different positions of wheel on track. At each position, the position of the wheel with respect to the rail is measured by finding the distance between the outer edge of the wheel and the rail as shown in Fig. 14. The edge to edge distance for all the positions are shown in Tab. 3.

The experiment is done as follows. The wheel is first jacked up using a lifting jack as shown in Fig. 13(b). The pressure measurement film is then placed on the rail's surface and secured with a tape and the wheel is lowered slowly until the lifting jack is fully loosened. The wheel is then allowed to rest on the film for about two minutes. Immediate removal of the wheel would lead to inaccurate results. After two minutes, the wheel is again raised from the surface by the lifting jack and the film is removed. The film is then scanned using a scanner and the post-processed using FPD-8010E software. Once the scanning is done, the software allows the user to select the region of contact patch for post-processing. In the post-processing, the user enters the minimum value of pressure below which the film cannot produce results. The

idea behind this step is to remove the area that represents the values below the minimum value from the contact patch. Since HHS films require higher pressure, they usually do not develop these erroneous patches. But it is very common in HS and MS films as they require very low value of pressure to develop a contact patch. Once the extra patch is removed, one can measure the dimensions of the patch using a cross arrow whose position is shown in a bar below the working area of the window.



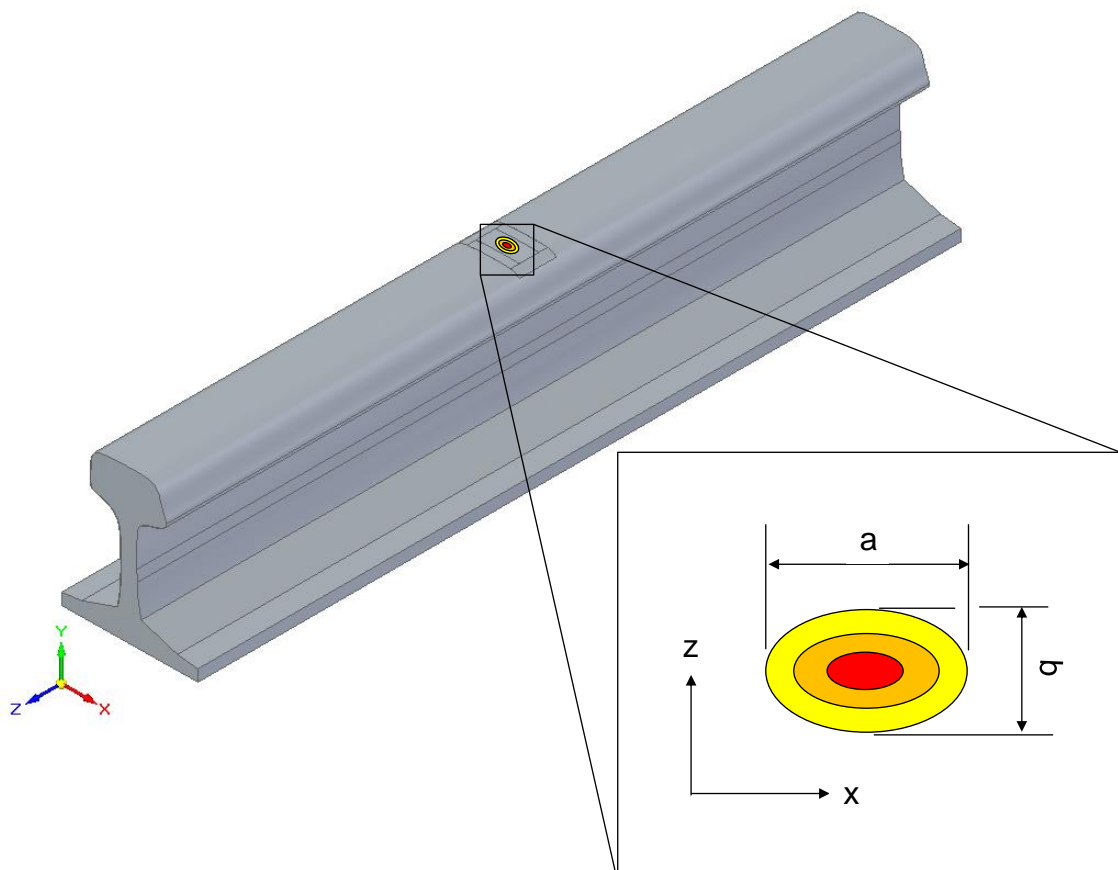
**Fig. 14: Distance between outer edges of rail and wheel**

**Tab. 3: Experiment positions and corresponding details**

Position	Wheel	Weight (in tonnes)	Edge to Edge distance (d) (in mm)
1	4	5.53	24.9
2	1	5.60	32.3
3	4	5.53	22.9
4	4	5.53	25.8

### 3.3 Results

The contact patches for all the four positions are obtained from experiments. The extents of the patches are measured and are named 'a' and 'b', which are the maximum lengths of the patch along x and z axis respectively. The maximum pressure and the pressure distribution inside the contact patch cannot be evaluated with pressure measurement films. Fig. 15 shows the parameters that are evaluated in experiments. According to [20], HHS films are affected by systematic error and thus, a correction value of  $-1.12 \pm 0.24$  must be applied to the extents of the contact patch. The dimensions of the contact patches and their shapes are shown in Tab. 4



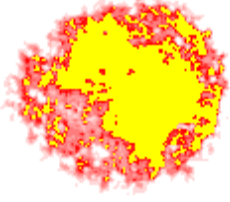
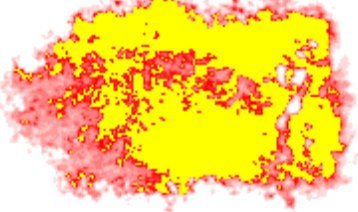
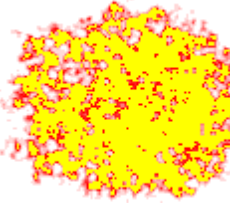
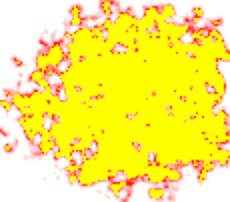
**Fig. 15: Measured parameters in experiments**

The contact patch of position 1 is almost circular. Whereas, for other three positions its completely non-Hertzian. Their shapes are almost oblong. Positions 1,3 and 4 have single point of contact but position 2 has a two-point contact. Initially, the points of contact are separated by a distance. As the load is applied the profiles grow symmetrically away from the points of contact and join to form a single contact patch. Also, the length 'a' of the contact patch for position 2 is almost twice its width 'b'. The yellow areas within the contact patch imply higher contact pressure compared to the red areas. Discontinuities in the yellow



patches show irregularities in the profiles of rail and wheel. The uniformity in the contact patches for positions 3 and 4 show the absence of surface irregularities. No contact patch has a well-defined contour. This can be attributed to low pressure sensitivity of HHS films.

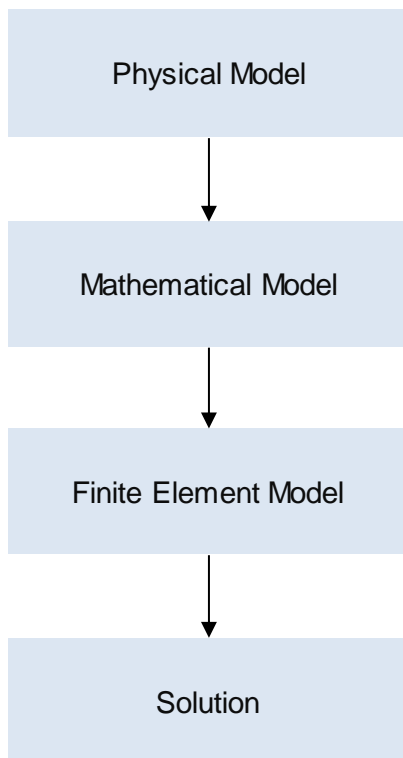
**Tab. 4: Details of contact patches obtained from experiments (extents with correction)**

Position	$a \pm 0.24$ (in mm)	$b \pm 0.24$ (in mm)	Field Side	Shape	Track side
1	12.13	10.88			
2	20.51	11.88			
3	13.38	11.13			
4	10.63	12.38			



## 4 Modelling and Simulation

For this thesis, the finite element mesh is created using Hypermesh 2017 software and the simulation and post processing is done using Abaqus CAE Standard 2017 and Abaqus Viewer softwares respectively. The model building process for this thesis is shown in Fig. 16. The physical model is first studied and a mathematical model is created. The mathematical model is then converted to FE model and the solution is obtained subsequently.



**Fig. 16: Modelling flow chart**

### 4.1 Physical Model

The actual physical model consists of a bogie with four independent wheels and a track as shown in Fig. 13(a). The track is broad gauge and the rails have 49E2 profile. Since the profiles of both the rails and wheels are worn out, their drawings cannot be used for CAD model creation. Thus, Nextsense's CALIPRI measurement device is used to measure both the wheel and rail profiles. The CALIPRI measurement device is shown in Fig. 17(a).

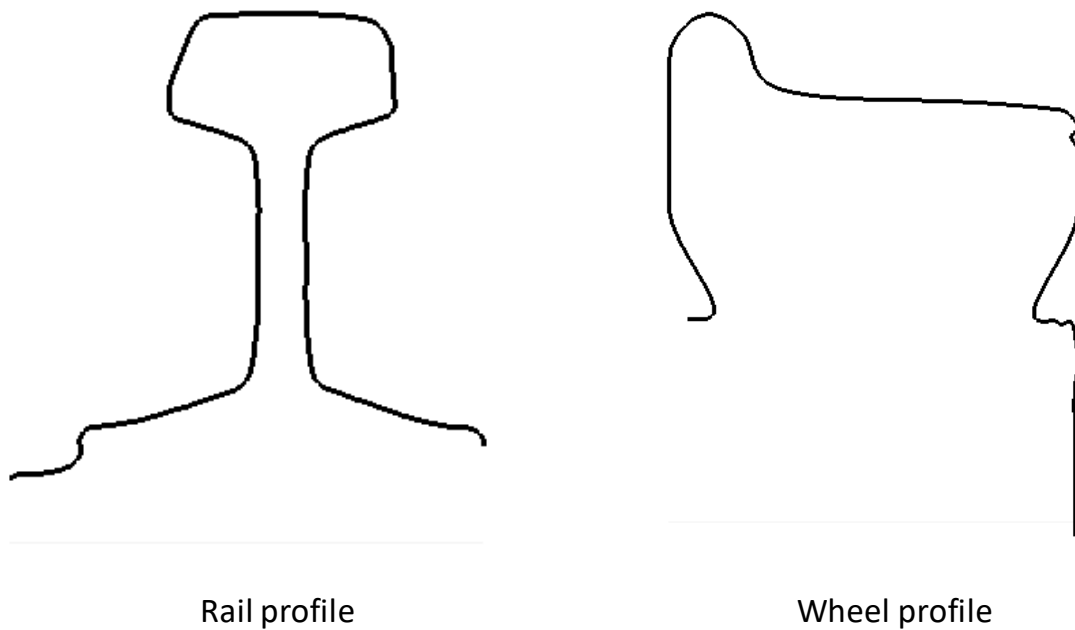


**Fig. 17: CALIPRI profile and diameter measurement devices [21] [22]**

The device consists of a tablet with specialized software installed in it. The tablet is connected to a device that emits laser to measure the profile through wire. The object to be scanned for measurement can be chosen in the software's GUI. For example, if a rail needs to be scanned, then the rail profile measurement program is chosen and parameters like the type of rail (Ex: 49E2) and width are entered. Once the measurements are done, the profiles can be exported and viewed in computer. The obtained profile data is in the form of point cloud which can be converted to 2D profile using CAD software. An example of the measured wheel and rail profiles are shown in Fig. 18.

The measurement of the diameters of the wheels however needs an auxiliary measuring device as shown in Fig. 17(b). This special device from CALIPRI is in the shape of a bow and has some cylindrical projects on it. These projections are aligned with the circumference of the wheel and secured by turning on a knob that activates an electromagnet. The measurements are then taken with the CALIPRI measurement device. The device calculates both the flange diameter and the rolling circle diameter of the wheel.

The Flange diameter of Wheel 1 and 4 are 964.67 mm and 931.25 mm respectively. Since the experiment involves measurements at four different positions, the rail profiles at all the four positions are recorded. The height of the rails is 140 mm. By design the 49E2 rail has a height of 148 mm. This implies that the rails have worn out by 8 mm approximately.

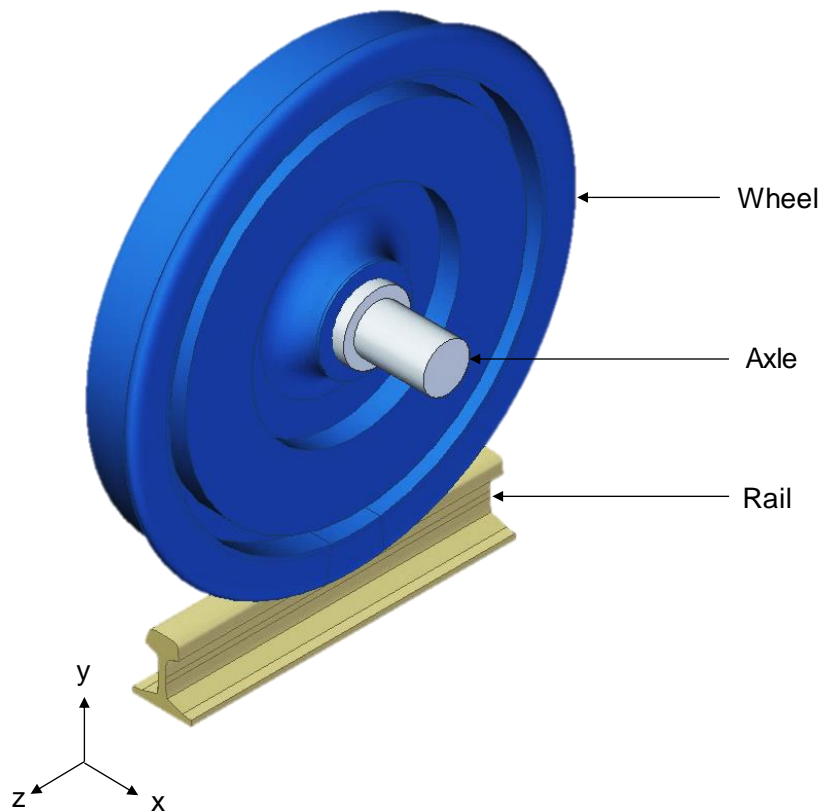


**Fig. 18:** Rail and wheel profiles measured with CALIPRI profile measurement device

## 4.2 Mathematical Model

Before simulations, it is crucial to consider the uncertainties in the boundary conditions, material behavior and geometric assumptions. In this step, the model is parametrized and a standard deviation is applied to the uncertainties. The mathematical model of the problem is cut short to the wheel, the rail and the axle. The Young's moduli of the wheel steel and rail steel are 209000 MPa and 208000 MPa respectively. The Poisson's ratio of both the materials is 0.29. The Young's modulus and the Poisson's ratio are not parametrized since their effect on results is negligible. The Axle is assumed to have same material as the wheel. The mathematical model is shown in Fig. 19. From the experiments, the loads at wheel 1 and 4 are 55799 N and 55101 N respectively. Considering possible error in the measuring scale, it is assumed that the forces have a standard deviation of  $\pm 1500$  N. The consistency in contact patches in experiments proves that, for the above loads, the material behaves linear elastic. The experiments are carried out at four different lateral positions of wheel and rail. Since the lateral position of the wheel with respect to the rail is manually measured between the curved edges of the wheel and rail, the uncertainties in the measurement needs to be considered. Thus, the lateral positions ( $u_x$ ) are assigned with a standard deviation of  $\pm 1$  mm. The inclination between tape circle plane and the rail center plane in the xy-plane ( $\phi_z$ ) is 1:40 ( $1.43^\circ$ ). Also, the wheels 1 and 4 are inclined with respect to yz-plane due to their difference in their rolling circle diameters. The inclination is calculated as  $0.69^\circ$ . Thus, the total inclination in xy plane would be  $1.43 \pm 0.69^\circ$  depending on the wheel. For this inclination, a

standard deviation of  $\pm 0.5^\circ$  is chosen. The list of factors with their normal distribution is given in Tab. 5.



**Fig. 19: Mathematical model**

**Tab. 5: Factors with normal distribution**

Factor	Mean value				Standard Deviation	Unit
	Position 1	Position 2	Position 3	Position 4		
P	55101	55799	55101	550101	1500	N
$\phi_z$	2.12	0.74	2.12	2.12	0.5	Degrees ( $^\circ$ )
$u_x$	24.9	32.3	22.9	25.8	1	mm

### 4.3 Finite Element Model

The mathematical model forms the basis for the Finite Element simulations. The FE model also consists of an axle, a wheel and a rail except that the wheel and rail are divided into inconsistent sub-domains as shown in Fig. 20. The mesh size changes with the sub-domain. This allows fine meshing in the regions of interest like the contact where accurate results are required and coarse meshing of regions like the main wheel sub-domain where accurate results are not necessary. The choice and order of elements also varies with respect to region meshed, as it is critical in emulating the physics of the problem. The geometry, mesh, boundary conditions and the loading for all the sub-models are discussed below.

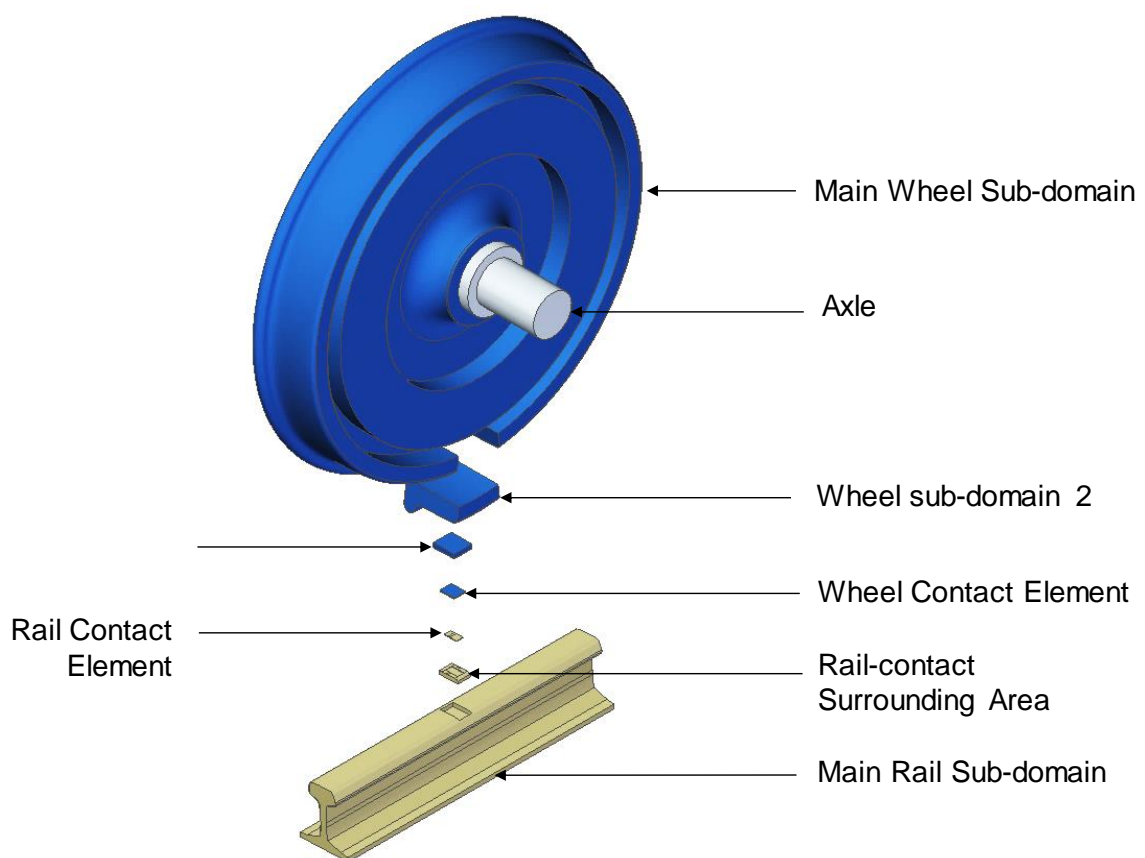


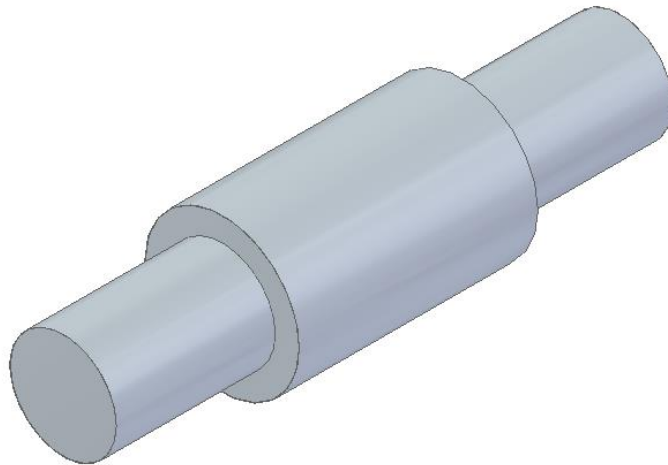
Fig. 20: Discrete regions of FE model

#### 4.3.1 The Axle

##### Geometry

The Axle model consists of a wheel-journal with two auxiliary journals in its sides. The length and diameter of the wheel-journal are 225 mm and 145 mm respectively. The auxiliary journals are 150 mm long and have a diameter of 100 mm. As the load is applied on the surface of auxiliary journals, it is transferred to the wheel journal and the wheel-journal relays

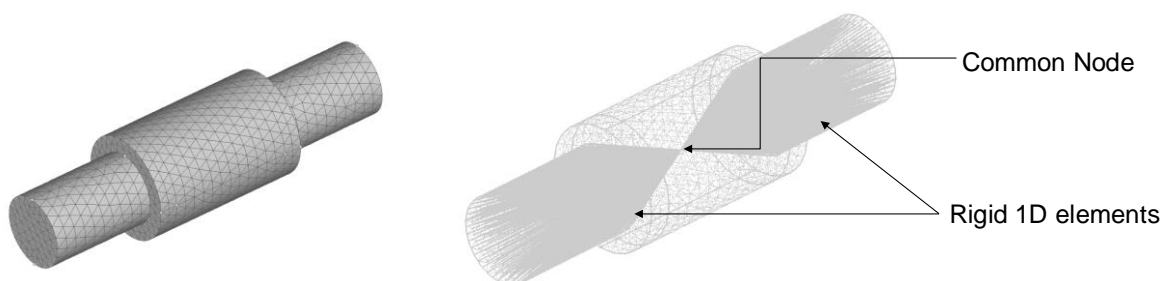
the load to the wheel and further through its bearing surface. The axle model is shown in Fig. 21.



**Fig. 21: Axle model**

### Mesh

The axle is meshed with quadratic tetrahedral elements (C3D10) with four integration points. These are second order elements and have ten nodes in total (four corner nodes and six mid side nodes). Second order elements are chosen as they exhibit better bending characteristics than first order tetrahedral elements. To emulate the actual loading, the surface nodes of the auxiliary journals are connected to a common node through a kinematic coupling. The load is applied on the common node and it is carried to the journal surfaces equally through the coupling. The mesh for Axle is shown in Fig. 22.

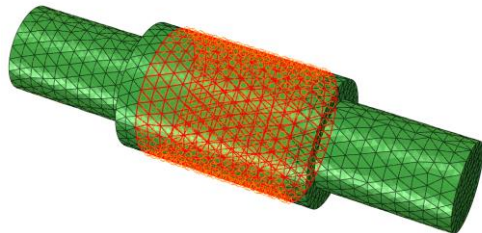
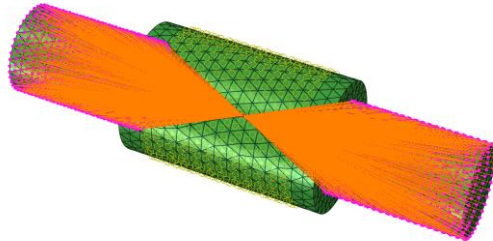
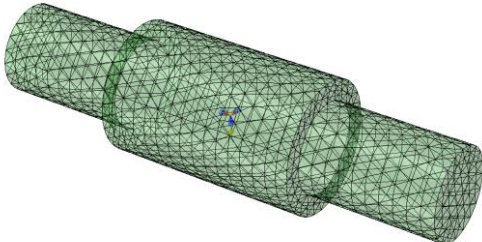


**Fig. 22: Axle mesh**

## Boundary conditions

The list of boundary conditions on the axle is shown in Tab. 6. The wheel-journal surface is connected to the wheel's bearing through a tie constraint. Tie constraint makes the bearing to follow the motion of the journal. All the degrees of freedom of the kinematic coupling are constrained. This allows it to act like a rigid coupling. The node to which the surface nodes of the auxiliary journals are connected can translate only along y-axis. All other degrees of freedom are arrested.

**Tab. 6: Boundary conditions on axle**

	Entity	Constraint
	Wheel-journal surface	Tie – with wheel bearing surface
	Kinematic coupling	$U1 = 0$ $U2 = 0$ $U3 = 0$ $UR1 = 0$ $UR2 = 0$ $UR3 = 0$
	Common node	$U1 = 0$ $U3 = 0$ $UR1 = 0$ $UR2 = 0$ $UR3 = 0$



## Loading

A concentrated load is applied on the common node. The value of force is parametrized and its nominal value depends upon the wheel used (i.e. 55101 N for wheel 4 or 55799 N for wheel 1). The load is applied in negative direction of the y-axis.

### 4.3.2 The Wheel

The wheel consists of four inconsistent sub-domains; The Main wheel sub-domain, Wheel sub domain 2, Wheel-contact surrounding area and the Wheel contact element. The sub-domains are connected to each other with tie constraints as shown in Fig. 23.

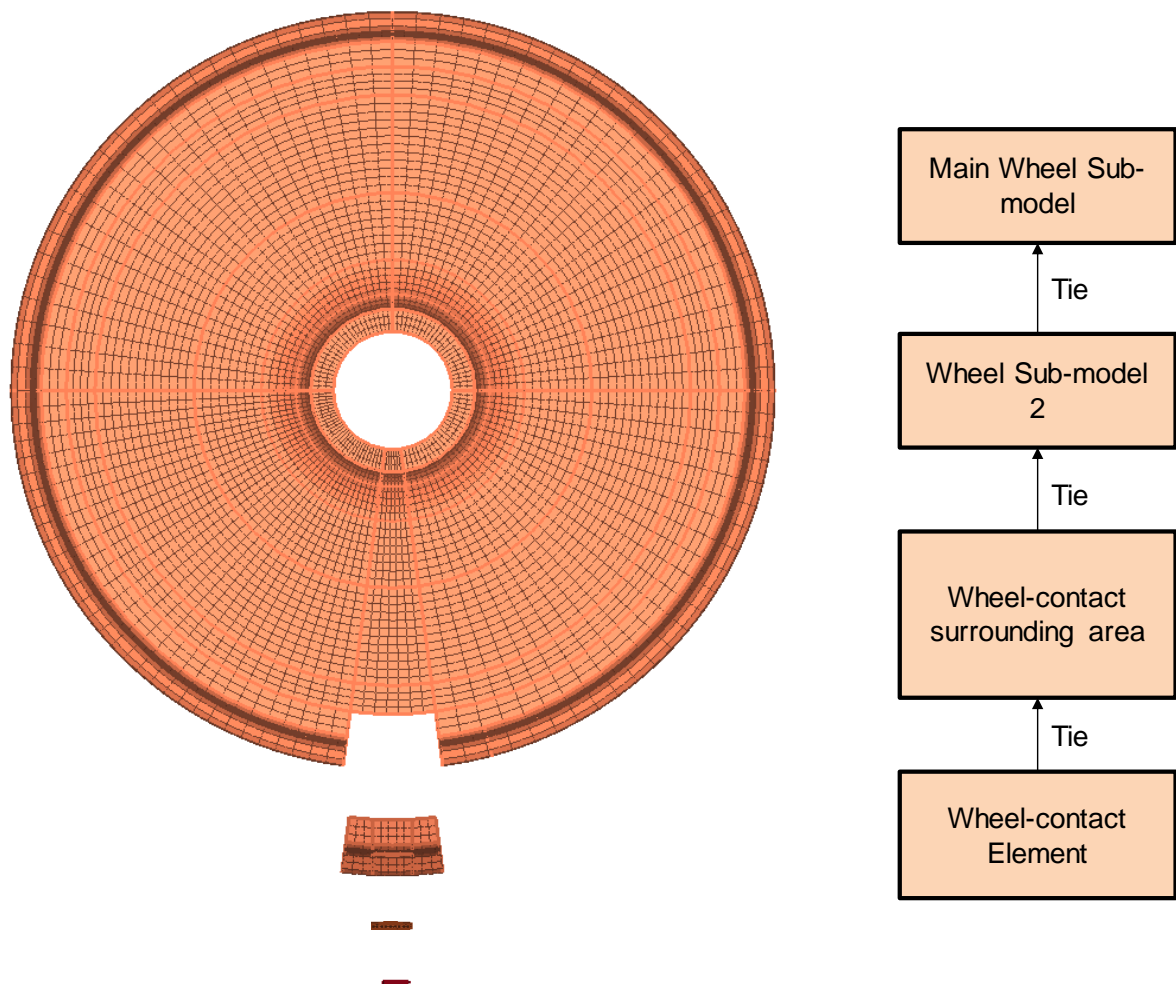


Fig. 23: Wheel model topology



### 4.3.2.1 Main Wheel Sub-domain

#### Geometry

For creating the 3D model for the Main wheel sub model, the dimensions of the cross section of the wheel is measured from the actual wheel and revolved about the axis of the wheel. The model is approximate as the dimensions are measured manually. The main profile of the wheel and the diameters (Flange diameter and Rolling circle diameter) are obtained from CALIPRI profile measuring device. Then a groove is cut on the wheel as shown in Fig. 24 to facilitate the placement of Wheel sub-model 2. The angle between the surfaces of groove is  $15^\circ$ .

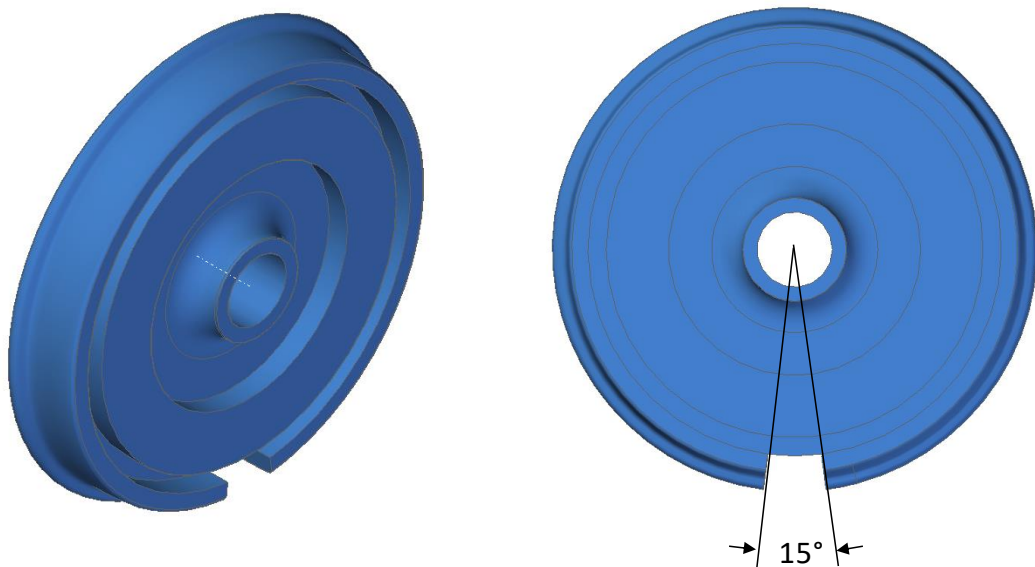


Fig. 24: Main wheel sub-domain geometry

#### Mesh

The Main wheel sub-domain is meshed with under-integrated quadratic hexahedral elements (C3D20R). These second order cuboidal elements are composed of 20 nodes (8 nodes at the corners and 12 mid-side nodes). Their shape functions are also quadratic. The element size is 15 mm in all the regions except in the sector above the slot where the element size is 10 mm as shown in Fig. 25.

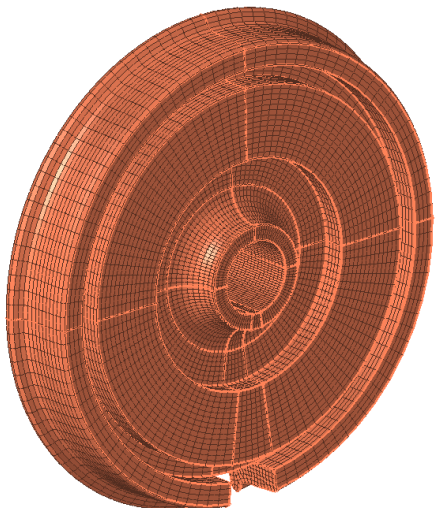
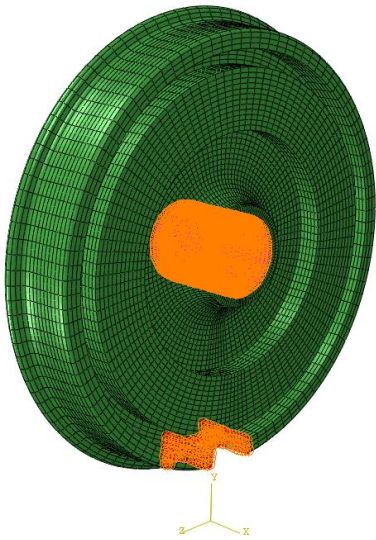
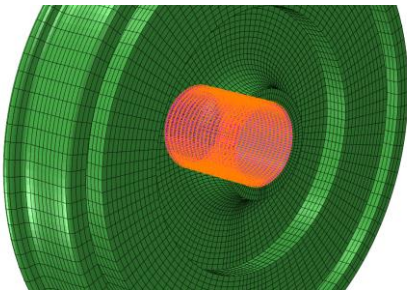
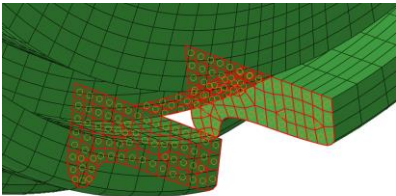


Fig. 25: Main wheel sub-domain mesh

Boundary Conditions

The boundary conditions for the Main wheel sub-domain are shown in Tab. 7. The bearing surface is tied to the axle’s journal surface and the groove is tied to wheel sub-model 1.

Tab. 7: Boundary conditions on Main wheel sub-domain

		Entity	Constraint
		Bearing surface	Tie – With Axle journal surface
		Groove	Tie – With Wheel sub-model 2

### 4.3.2.2 Wheel Sub-domain 2

#### Geometry

The geometry of wheel sub-domain 2 is obtained by rotating a part of wheel's cross section up to  $15^\circ$  about the axis of the wheel as shown in Fig. 26, so that it perfectly fits the groove in the Main wheel sub-model. A slot is cut-out on the outer surface to accommodate the contact surrounding area. The slot is positioned and designed to capture the contact patch with minimal contact elements.

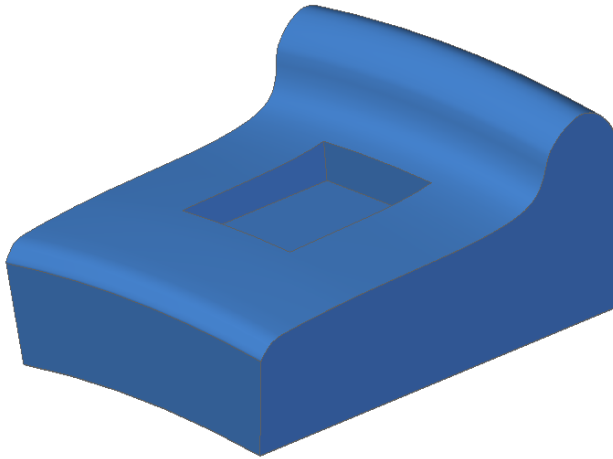


Fig. 26: Wheel sub-domain 2 geometry

#### Mesh

Like the Wheel Main sub-domain, this sub-domain is also meshed with under-integrated quadratic hexahedral elements (C3D20R) as shown in Fig. 27. A constant mesh size of 10 mm is maintained throughout the model.

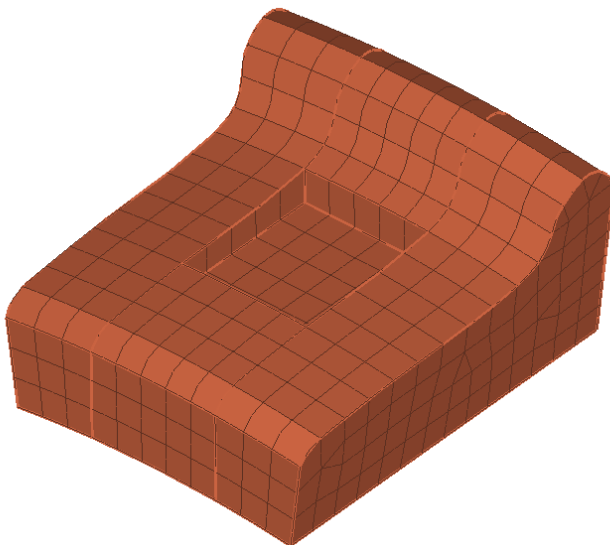
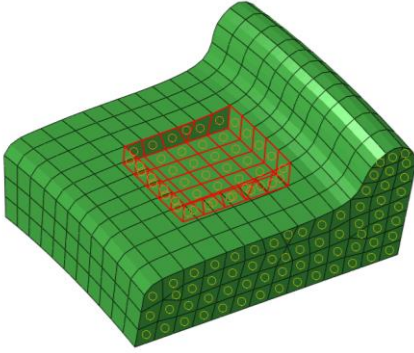
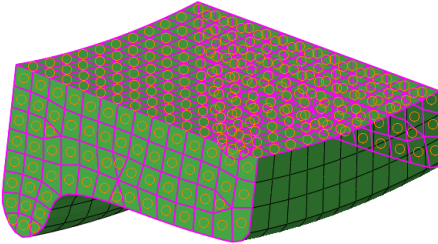


Fig. 27: Mesh for Wheel sub-domain 2

### Boundary Conditions

The boundary conditions for Wheel sub-domain 2 is shown in Tab. 8. The slot is tied to the Wheel-contact surrounding area and the bottom and sides are tied to groove in the Main wheel sub-domain.

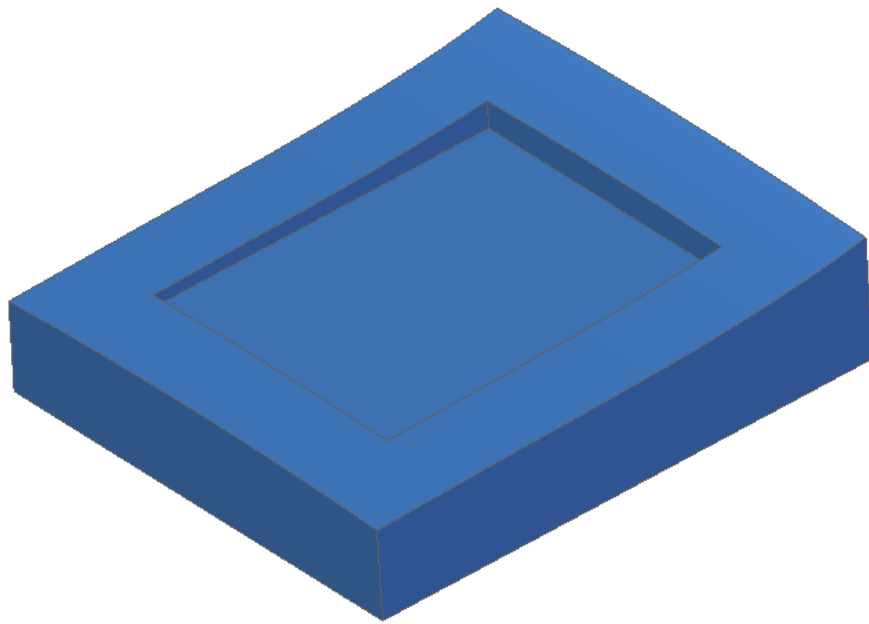
**Tab. 8: Boundary conditions on Wheel sub-domain 2**

	Entity	Constraint
	Slot	Tie – With Wheel-contact surrounding area
	Bottom and sides	Tie – With bottom and sides of the groove in Main wheel sub-domain

#### 4.3.2.3 Wheel-contact Surrounding Area

##### Geometry

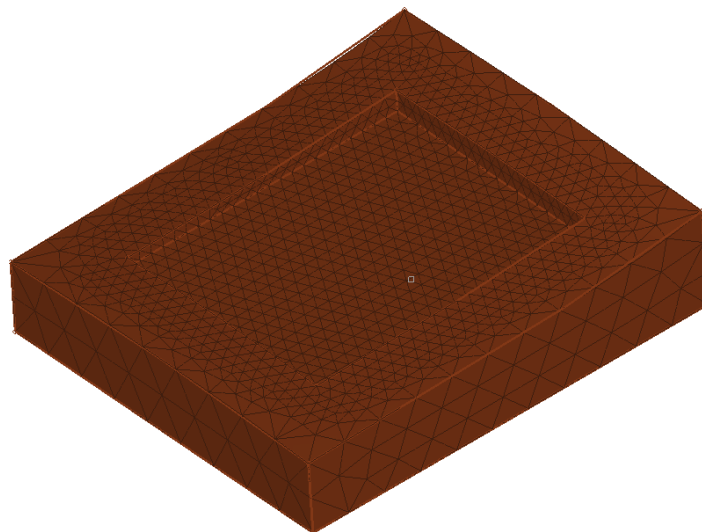
The geometry of the contact surrounding area is designed to fit the slot in the wheel sub-domain 2. A slot is cut-out on its surface to contain the contact element. A thick wall is built around the slot to provide a gradient in the mesh. The geometry of the Wheel-contact surrounding area is shown in Fig. 28.



**Fig. 28: Geometry of Wheel-contact surrounding area**

### Mesh

The quadratic tetrahedral elements (C3D10) are used for meshing wheel-contact surrounding area. A gradient is created in the mesh to improve the accuracy of the solution. The element size on the surfaces of the slot is 1.6 mm and the element size on the outer surfaces of the body is 5 mm. Thus, the element size is gradually increased from 1.6 mm up to 5 mm within the body. The idea is to provide each node in the parent body with at least 2 nodes in child for the tie constraint. The mesh for Wheel-contact surrounding area is shown in Fig. 29.

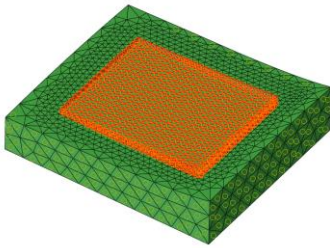
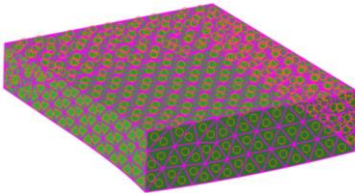


**Fig. 29: Mesh for Wheel-contact surrounding area**

### Boundary Conditions

The boundary conditions for the wheel-contact surrounding area is shown in Tab. 9. The slot nodes are tied with the wheel contact element and the bottom and sides are tied to slot in the Wheel sub-domain 2.

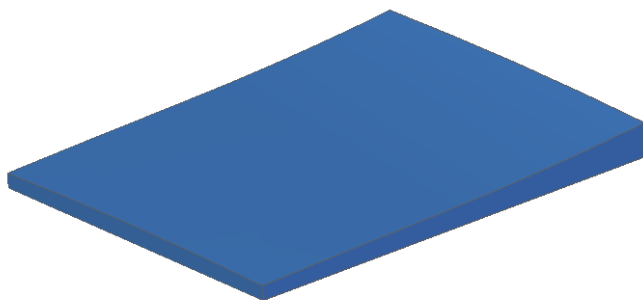
**Tab. 9: Boundary conditions on Wheel-contact surrounding area**

	Entity	Constraint
	Slot	Tie – With Wheel contact element
	Bottom and sides	Tie – With sides of the slot in Wheel sub-domain 2

#### 4.3.2.4 Wheel Contact Element

##### Geometry

The geometry of the contact element exactly fits the slot in the Wheel-contact surrounding area. The geometry is designed to accommodate at least four rows of elements along its thickness. The geometry of the contact element is shown in Fig. 30.



**Fig. 30: Geometry of Wheel contact element**

Mesh

The under-integrated linear hexahedral elements (C3D8R) are used for meshing the contact element. The element size for contact element needs to be small enough to capture the contours of the contact patch accurately. Thus, an element size of 0.3 mm is maintained throughout the body. The meshed contact element is shown in Fig. 31.

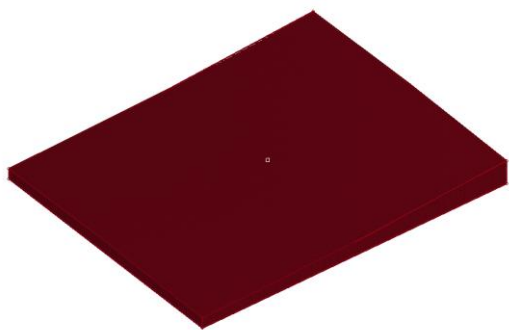
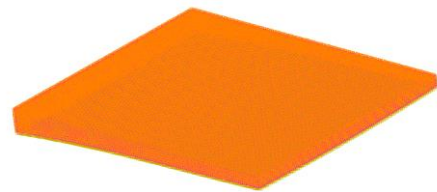
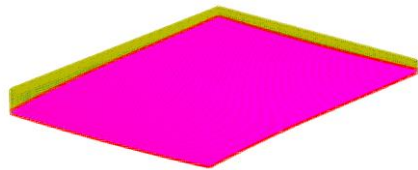


Fig. 31: Meshed Wheel contact element

Boundary Conditions

The boundary conditions for the wheel contact element is shown in Tab. 10. The nodes in the bottom and sides are tied to slot in Wheel-contact surrounding area. In addition to that, the top surface of the contact element is defined as the slave surface of the contact pair.

Tab. 10: Boundary conditions on Wheel contact element

	Entity	Constrains
	Bottom and sides	Tie – With surfaces of the slot in Wheel-contact surrounding area
	Top surface	Slave



### 4.3.3 The Rail

The Rail is divided into three sub-domains; The Main rail sub-domain, Rail-contact surrounding area and The Rail contact element. The inconsistent sub-domains of rail are connected to each other with tie constraints as in shown in Fig. 32.

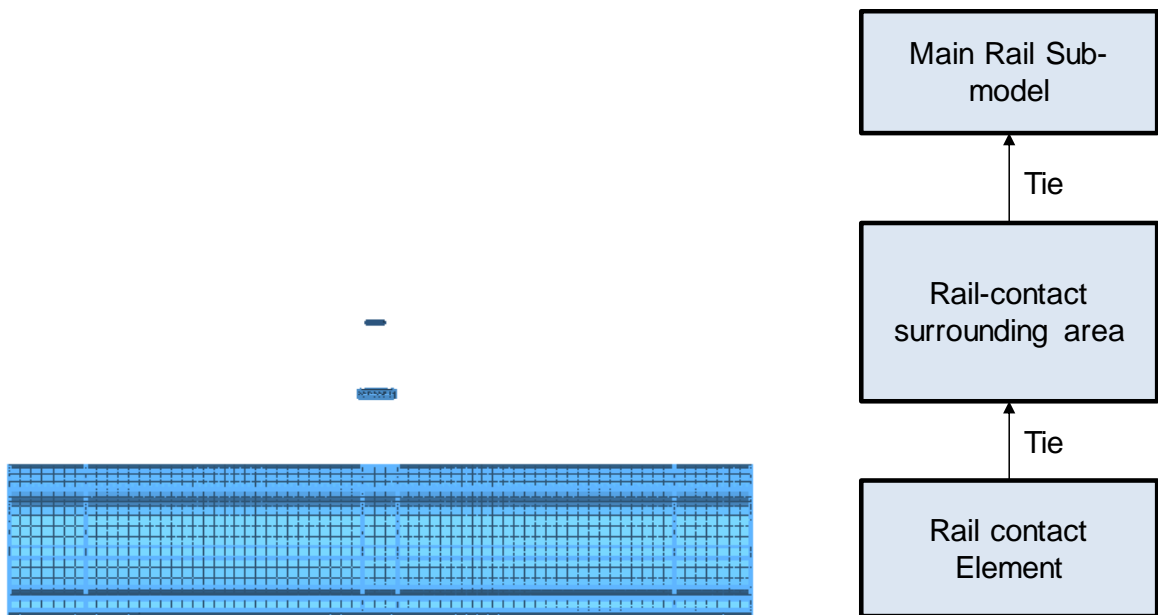


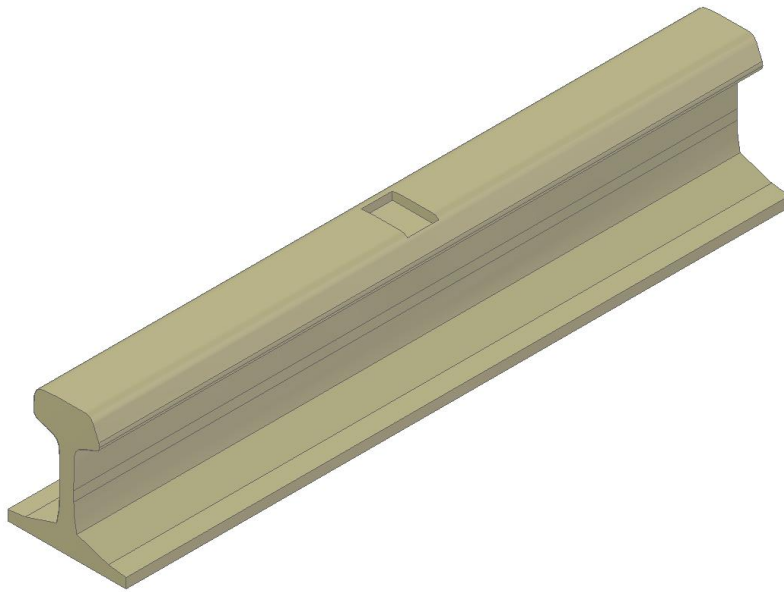
Fig. 32: Rail model topology

#### 4.3.3.1 Main Rail Sub-domain

##### Geometry

The main rail sub-domain model is obtained from extruding the rail profile obtained from the CALIPRI rail profile measurements. The length of the rail is reduced to 700 mm, which is the distance between the centers of two successive sleepers in the track. A cuboidal slot is made at the center of the rail to insert other sub-models. The size of the slot is kept different for different wheel-rail positions to track the contact patch with minimal use of contact elements in simulations. The position of the contact determines the size of the slot. The geometry of main rail sub-domain is shown in Fig. 33.

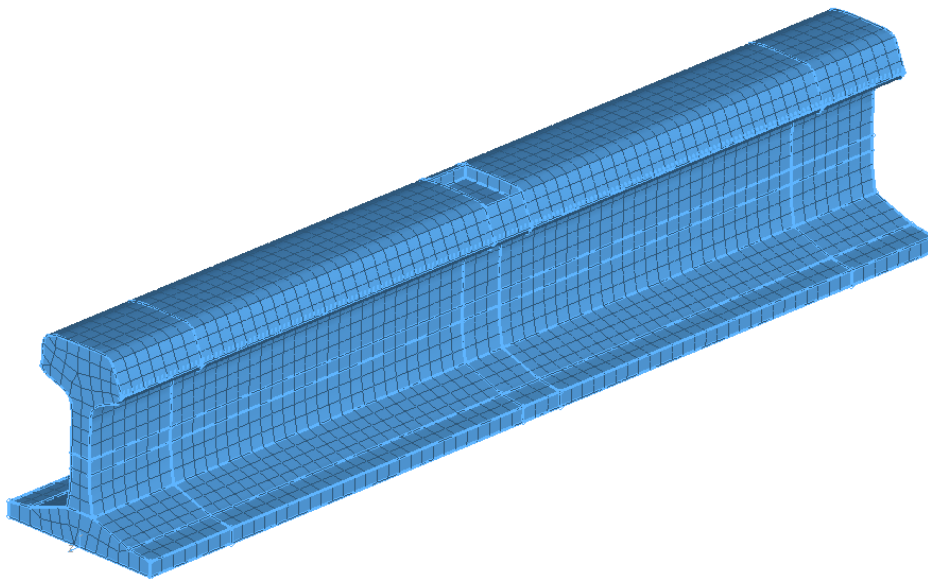




**Fig. 33: Main rail sub-domain model**

### Mesh

Since the rail is “simply supported” at the sleepers, it would bend downwards at the center along the yz-plane as the load is applied. Thus, for meshing the Main rail sub-domain, under-integrated quadratic hexahedral elements (C3D20R) are used, as they exhibit better bending characteristics compared to first order hexahedral elements. A constant size of 10 mm is maintained throughout the model. The mesh for the Main rail sub-model is shown in Fig. 34.

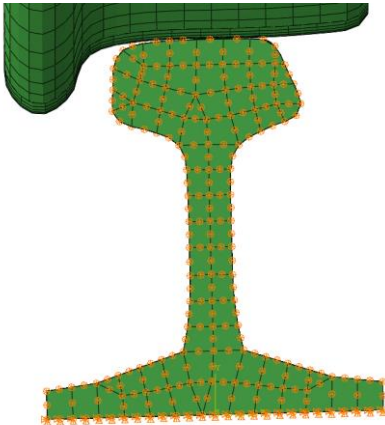
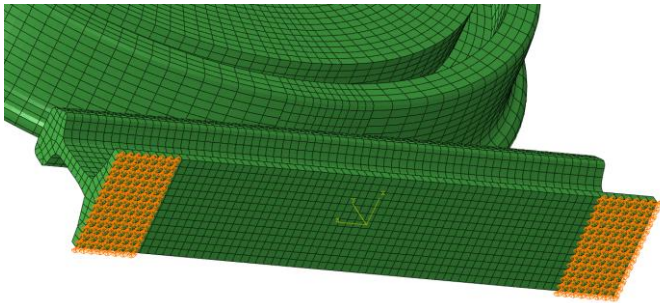
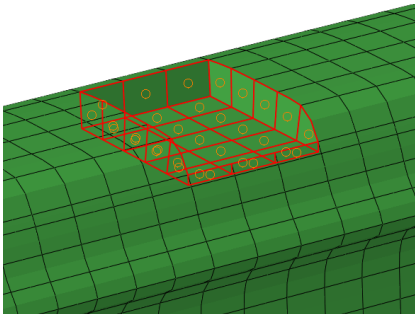


**Fig. 34: Main rail sub-model mesh**

## Boundary Conditions

The railway track is laid on equally spaced sleeper blocks throughout its length. Between the rail and the sleepers lies a rectangular Tie plate. It is used to increase the bearing area and to fasten the rail to its position. The width of the plate is around 145 mm. Since the length of the rail considered for the simulations is the distance between the centers of two successive sleepers, the rail is fixed (in all translatable degrees of freedom) at the bottom up to 72.5 mm from both the ends as shown in Tab. 11.

**Tab. 11: Boundary conditions on Main rail sub-model**

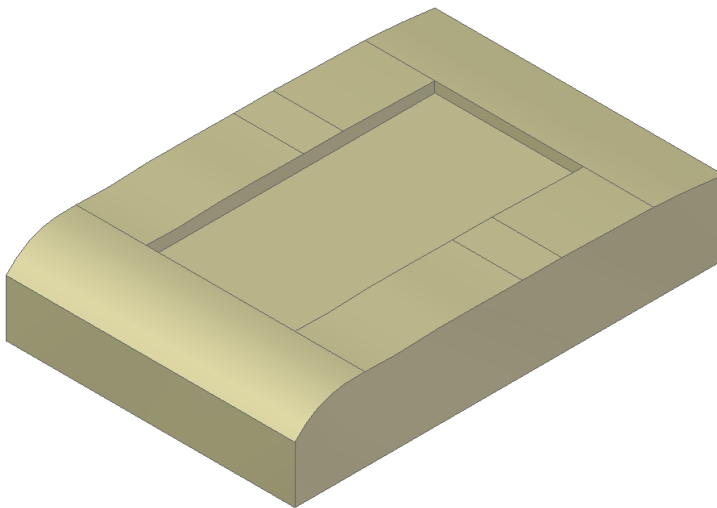
	Entity	Constraint
	Rail sides	$U_3 = 0$
	Rail bottom	$U_1 = 0$ $U_2 = 0$ $U_3 = 0$
	Slot	Tie – with Rail-contact surrounding area

The sides of the wheel are fixed in translatory  $z$  direction to emulate the infinite length of the rail. The elements that belong to the surfaces of the slot are tied to the elements on the Rail-contact surrounding area that are adjacent to the slot.

#### 4.3.3.2 Rail-contact Surrounding Area

##### Geometry

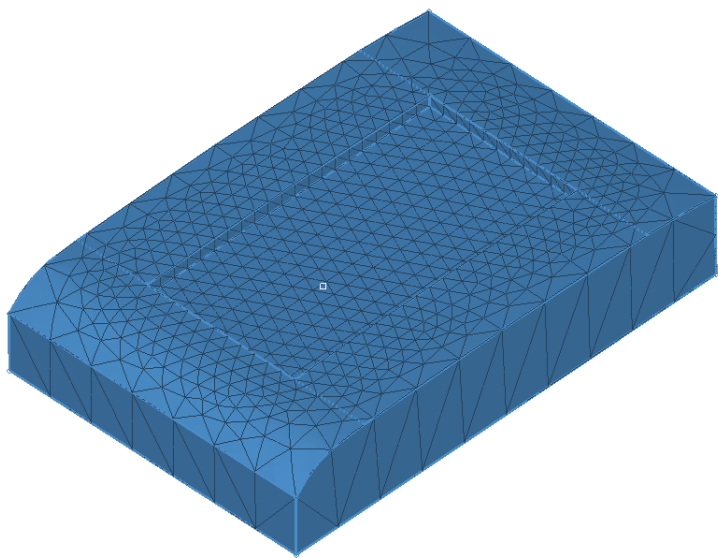
The geometry of the contact surrounding area exactly fits the slot in the main rail sub-domain. The element also consists of a thin slot to contain the contact element. The size of the slot is designed in a way that the contact element has at least four elements along its thickness. A constant wall thickness is maintained around slot. The geometry of the Rail-contact surrounding area is shown in Fig. 35.



**Fig. 35:** Rail-contact surrounding area

##### Mesh

Like the Axle and the wheel-contact surrounding area, this element is also meshed with the quadratic tetrahedral elements (C3D10) as shown in Fig. 36. The mesh size is same as in the wheel-contact surrounding area. Similar gradient pattern is created in mesh to improve the accuracy of the solution.



**Fig. 36: Mesh for Rail-contact surrounding area**

**Boundary Conditions**

The boundary conditions for the Rail-contact surrounding area are shown in Tab. 12. The bottom and sides are tied with the slot surfaces in the main wheel sub-domain and the slot surfaces are tied with the contact element.

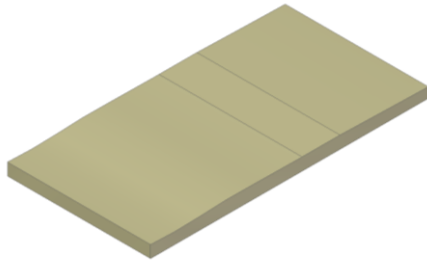
**Tab. 12: Boundary conditions on Rail-contact surrounding area**

	Entity	Constraint
	Slot	Tie – With Contact element
	Bottom and sides	Tie – With sides of the slot in Main rail sub-model

### 4.3.3.3 Rail Contact Element

#### Geometry

The design of the rail contact element is similar to that of wheel's as shown in Fig. 37. The geometry exactly fits the slot in the contact surrounding area element.



**Fig. 37: Geometry of Rail contact element**

#### Mesh

As in the wheel contact element, the rail contact element is meshed with the under-integrated linear hexahedral elements (C3D8R) as shown in Fig. 38. The size of the elements is also 0.3 mm as in the wheel contact element.


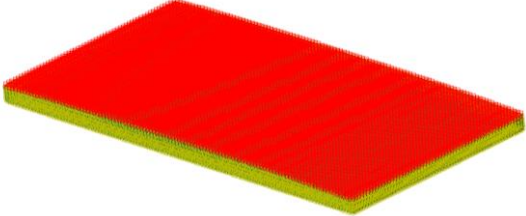


**Fig. 38: Rail contact element mesh**

#### Boundary Conditions

The boundary conditions for the Rail contact element is shown in Tab. 13. The nodes in the bottom and sides are tied to slot in the Rail-contact surrounding area. In addition to that, the top surface of the contact element is defined as the master surface of the contact pair

**Tab. 13: Boundary conditions on Rail contact element**

	Entity	Constraint
	Bottom and sides	Tie – With surfaces of the slot in Rail-contact surrounding area
	Top surface	Master

#### 4.3.4 Simulation Settings

Meshing, material property creation, section assignment, element and node set creation and other preliminary tasks are done in Hypermesh. As the first step, the input file containing the mesh created using Hypermesh 2017 software is imported into ABAQUS CAE. The input file contains all the above-mentioned data coded into it. The simulations are done with Abaqus Standard FE solver in implicit dynamic quasi-static mode. The total time for the simulation is one. The initial and maximum increment sizes are 0.01 and  $1e^{-05}$  respectively. The maximum number of increments is 100.

“Full Newton” solution technique is selected with default matrix storage system. Surface to Surface contact discretization has been chosen for this problem. The top surface of the Rail contact element has been chosen as the master surface and the top surface of the Wheel contact element has been chosen as the slave. The augmented lagrange contact formulation with “Hard Contact” pressure overclosure is selected for the normal direction. Other settings like contact stiffness value, stiffness scale factor and clearance at which contact pressure is zero are left default. Pure penalty formulation is selected for the tangential direction with a friction coefficient of 0.3. Other settings in the friction, shear stress and elastic slip tabs are left default.

### 4.3.5 DOE Setup

As discussed in the mathematical model, each factor has been assigned with a standard deviation and for every factor there are three levels; the Nominal, Maximum and Minimum. For this problem, the full factorial model has been chosen. Since we have three factors (Force, Rail inclination and the Lateral position) and three levels, the total number of simulation would be 27 ( $=3^3$ ). For simplification, only two levels (minimum and the maximum) are first taken into consideration and a simulation with nominal values of all the factors is added to the DOE. Thus, we have 9 ( $=2^3+1$ ) simulations in total. The list of simulations to be done for each position is listed below in Tab. 14. The 0, +1 and -1 are the nominal, maximum and minimum values respectively. Other simulations are done if desired results are not obtained from these simulations.

**Tab. 14: List of simulations for DOE**

Simulation Number	Force (P)	Rail Inclination ( $\phi_z$ )	Lateral Position ( $u_x$ )
1	0	0	0
2	+1	-1	-1
3	+1	-1	+1
4	+1	+1	-1
5	+1	+1	+1
6	-1	-1	-1
7	-1	-1	+1
8	-1	+1	-1
9	-1	+1	+1

## 5 Results and Discussion

The simulation results are obtained and the contact patch dimensions are measured. For all the positions, the first five simulations of the DOE set up are carried out initially. If the shape of the contact patch obtained from one or more of these simulations has a good agreement with the experimental result, they are repeated again with higher value of force as it could alter the extents. The contact patch with shows good agreement both in shape and size is chosen as the best result. If the contact patches obtained from first five simulations are not acceptable, then the DOE is extended with simulations containing combinations of a  $3^3$  full-factorial design. In this case, simulations six to eight are not carried out since force does not influence the shape of the contact patch.

### Position 1


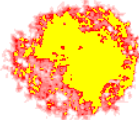







The list of obtained contact patches at different trials for position 1 are shown in Tab. 15. Initially the contact patch is triangular. The shape changes as we change the values of the factors. The first simulation is done with nominal values of force, rail Inclination and lateral position. The obtained contact patch is triangular and dissimilar to contact patch obtained from experiments. The extent in z-direction is greater than the extent in x-direction. Simulations two, three, four and five are done with the lower level of force. The levels of the other factors are varied between +1 and -1. The contact patch obtained from the second simulation has two detached regions. One has a triangular shape and other has an oval shape. This clearly shows that the positioning of wheel with respect to rail is incorrect for this simulation. The contact patch obtained from the third simulation looks similar to the contact patch obtained from experiments. The extent along x-axis is larger than the extent in z-direction. However, the shape of the contact patch does not exactly match with the one obtained from the experiments. The contact patches of simulations four and five have an oval shape with the extent in z-direction greater than the extent in x-direction. Since the simulation results do not match with experimental results, the DOE is extended further with simulations containing combinations of the  $3^3$  factorial design. The sixth, seventh and the eighth simulation are carried out with nominal value of lateral position and 'low' value of rail inclination. Out of these, the experiment number seven shows good agreement with the contact patch obtained from the experiments. The contact shape matches with the one obtained from the experiments. Though the other two contact patches show good agreement in shape, the extents do not match the experimental results.

The contact area obtained from simulation number seven is oblong as shown in Tab. 16. The contact patch is obtained at 'low' level of the applied force (53601 N) and the rail inclination ( $1.62^\circ$ ) and nominal lateral position (24.9 mm). The contact patch is slightly longer along x-axis compared to its extent in z-axis. The contact patch is continuous, realistic and without any split contact areas like in real case. This is due to smoothing of the rail and wheel profiles before the CAD model creation. It is a single point contact and the maximum



pressure obtained for this configuration is 794.6 MPa. The extent ‘a’ of the contact patch is closer to the value obtained in experiments, but the extent ‘b’ is smaller than the experimental value.

Tab. 15: Outcomes of simulations for position 1

Sim. No.	Force (P)	Rail Inclination ( $\phi_z$ )	Lateral Position ( $u_x$ )	Contact Patch	Contact patch from experiment
1	0	0	0		
2	-1	-1	-1		
3	-1	-1	+1		
4	-1	+1	-1		
5	-1	+1	+1		
6	0	-1	0		
7	-1	-1	0		
8	+1	-1	0		

Tab. 16: Details of contact patches obtained from simulations and experiment for position 1


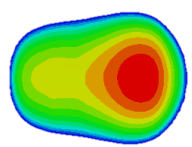
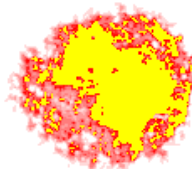
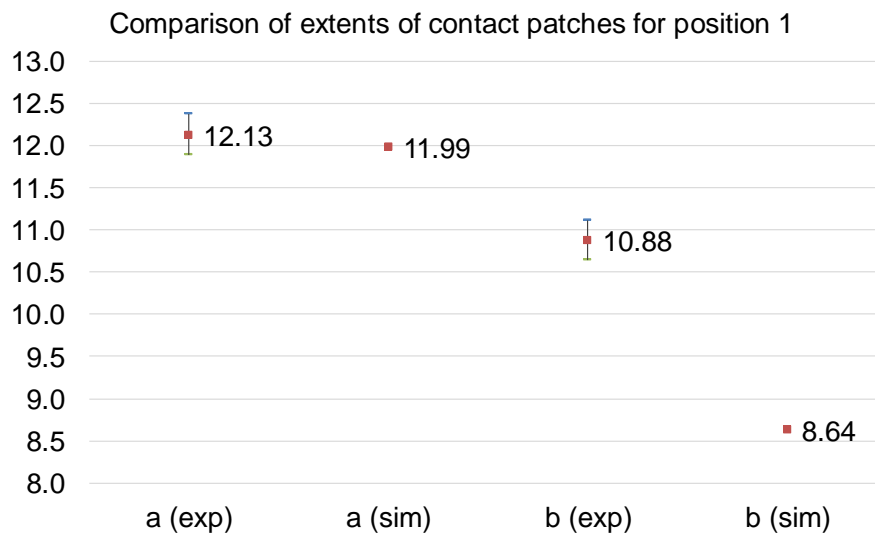
	a (in mm)	b (in mm)		Contact Patch	
Simulation Result	11.99	8.64	Field Side	Contact Status (CSTATUS)	Track side
					
Experiment result	12.13 ±0.24	10.88 ±0.24	Field Side	Contact Pressure Distribution (CPRESS)	Track side
					
					

Fig. 39 (a) shows the comparison between the extents of the contact patches obtained from the simulations and experiment for position 1. The results show that the extent ‘a’ of the contact patch obtained from the simulation is closer to the value obtained from the experiment and within the tolerance range of the experimental value. But the extent ‘b’ is approximately 2.3 mm lesser than the experimental value and not within the tolerance range.



**Fig. 39: Comparison of extents of contact patches obtained from simulations and experiment for position 1**

### Position 2


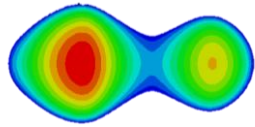
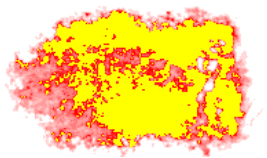
The list of obtained contact patches at different trials for position 2 are shown in Tab. 17. For this position, desired results are obtained with the initial five experiments itself. Therefore, it would be redundant to carry out other experiments.

**Tab. 17: Outcomes of simulations for position 2**

Sim. No.	Force (P)	Rail Inclination ( $\phi_z$ )	Lateral Position ( $u_x$ )	Contact Patch	Contact patch from experiment
1	0	0	0		
2	-1	-1	-1		
3	-1	-1	+1		
4	-1	+1	-1		
5	-1	+1	+1		

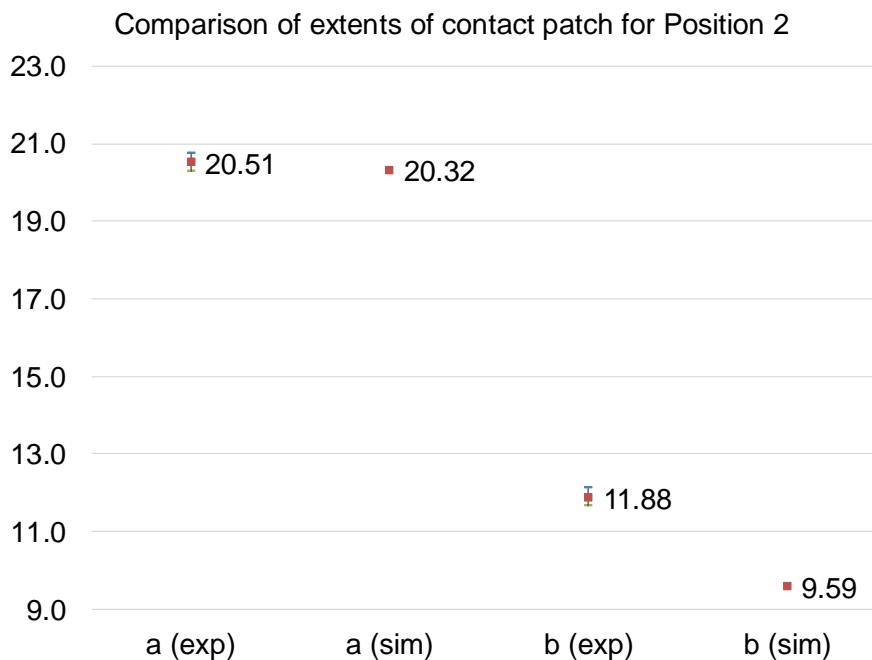
The first simulation is carried out with nominal values of all the factors. The other four simulations are carried out at the 'low' level of normal force and the values of other factors are varied between 'high' and 'low'. For all the performed simulations, the contact patches' extent in x-direction has invariably been larger than in z-direction. The contact patch obtained for the first simulation with nominal values of all the factors is oblong. Its extent in x-direction larger than the extent in z-direction. It is also a single point contact. The second simulation is done with 'low' levels of all the variables. The contact patch obtained is oval. Similar to the first simulation, the extent is bigger along x-axis than in z-axis. Initially when the contact is attained, the contact patch is elliptical with its major axis aligned with the z-axis. As the normal force increases, the contact patch expands in x-direction resulting in an oval shape. The contact patches obtained for the third and the fifth simulation are dissimilar to the experimental contact patch. The contact patches have a sharp vertical edge as the contact is partly outside the area of contact element. The contact patch for the fourth simulation has good agreement with the contact patch from the experiments. The contact patch obtained for this simulation is shown in Tab. 18. The contact patch is obtained at 'low' level of applied force (54299 N) and lateral position (31.3 mm) and 'high' level of rail inclination (1.24°).

**Tab. 18: Details of contact patches obtained from simulations and experiment for position 2**

	a (in mm)	b (in mm)		Contact Patch	
Simulation Result	20.32	9.59	Field Side	Contact Status (CSTATUS)	Track side
					
Experiment Result	20.51 ±0.24	11.88 ±0.24	Field Side	Contact Pressure Distribution (CPRESS)	Track side
					
Experiment Result	20.51 ±0.24	11.88 ±0.24	Field Side		Track side

The contact pressure distribution obtained from CPRESS output parameter shows that it is a two-point contact. The initial contact is attained at the left contact point. As the wheel deforms, the second contact point is obtained. Further deformation causes both the contact areas to merge. Like position 1, the contact patch has a larger extent in x-direction compared to the z-direction. Also, the extent 'a' is closer to the value obtained in experiments and the extent 'b' is smaller compared to the experimental value. The maximum contact pressure obtained for this position is 770 MPa, in the left contact point. The contact patch is continuous and realistic. There is no waviness or discrete patches within the contact patch.

Fig. 40 shows the comparison between the extents of the contact patches obtained from the simulation and the experiment for position 2. The results show that the extent 'a' of the contact patch obtained from simulation is closer to the value obtained from experiment and within the tolerance range of the experimental value. But the extent 'b' is approximately 2.3 mm lesser than the experimental value and not within the tolerance range.




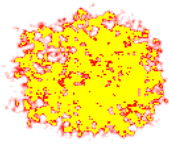




**Fig. 40: Comparison of extents of contact patches obtained from simulations and experiment for position 2**

### Position 3

The list of obtained contact patches at different trials for position 3 are shown in Tab. 19. None of the obtained contact patch shows good agreement with the one obtained from experiments. This can be attributed to wobbling of the wheel while carrying out the experiments. Wobbling causes an increase in the angular position of the wheel with respect to rail, making the rail inclination value to move out of the chosen tolerance value. This subsequently leads to incorrect contact patches. The contact for the first, fourth and fifth simulations are partly outside the area of contact element and the contact patch is dissimilar

to the one obtained from experiments. The contact patch for second and third experiments have an elliptical shape with their major axes aligned with the z-axis.


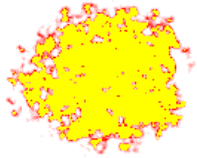





**Tab. 19: Outcomes of simulations for position 3**

Sim. No.	Force (P)	Rail Inclination ( $\phi_z$ )	Lateral Position ( $u_x$ )	Contact Patch	Contact patch from experiment
1	0	0	0		
2	-1	-1	-1		
3	-1	-1	+1		
4	-1	+1	-1		
5	-1	+1	+1		

#### Position 4

The list of obtained contact patches at different trials for position 4 are shown in Tab. 20. The first simulation is carried out with nominal values of all the factors. The other four simulations are carried out at 'low' level of normal force and the values of other factors are varied between 'high' and 'low'. The contact patch obtained is oblong for first three simulations like the experimental contact patch and oval for the fourth and fifth simulations. The extent of the contact patches in x-direction for the first three simulations is larger than the extent in z-direction. The first contact patch has its initial contact point near the field side and then tapers out towards the track side. But the experimental contact patch has its initial contact point near the track side and tapers out towards the field side. This feature can be seen in contact patches from simulations two and three. Out of these two simulations, simulation number three shows good agreement with the contact patch obtained from actual experiments. Thus, the simulation is repeated (experiment number six) with 'high' level of force to check its effect on the extents. The obtained contact patch shows good agreement by shape and size with the one obtained from experiments.

**Tab. 20: Outcomes of simulations for position 4**

Sim. No.	Force (P)	Rail Inclination ( $\phi_z$ )	Lateral Position ( $u_x$ )	Contact Patch	Contact patch from experiment
1	0	0	0		
2	-1	-1	-1		
3	-1	-1	+1		
4	-1	+1	-1		
5	-1	+1	+1		
6	-1	-1	0		

The contact patch for this simulation is oblong as shown in Tab. 21. The contact patch is obtained at 'low' level of applied force (53601 N) and rail inclination ( $1.62^\circ$ ) and nominal lateral position (25.8 mm). The contact pressure distribution obtained from CPRESS output parameter shows that it is a single point contact. The contact patch has a larger extent in x-direction compared to z-direction. Also, the extent 'a' is closer to the value obtained in experiments and the extent 'b' is smaller compared to the experimental value like in other positions. The maximum contact pressure obtained for this position is 908.3 MPa. The contact patch is continuous and realistic with no waviness or discrete patches within the contact patch. Fig. 41 shows the comparison between the extents of the contact patches obtained from simulations and experiment for position 2. The results show that the extent 'a' of the contact patch obtained from simulation is closer to the value obtained from experiment and within the tolerance range of the experimental value. But the extent 'b' is 2.2 mm lesser than the experimental value and not within the tolerance range.

Tab. 21: Details of contact patches obtained from simulations and experiment for position 4

	a (in mm)	b (in mm)	Field Side	Contact Patch	Track side
Simulation Result	10.47	10.18		Contact Status (CSTATUS)	
				Contact Pressure Distribution (CPRESS)	
Experiment Result	10.63 ±0.24	12.38 ±0.24			

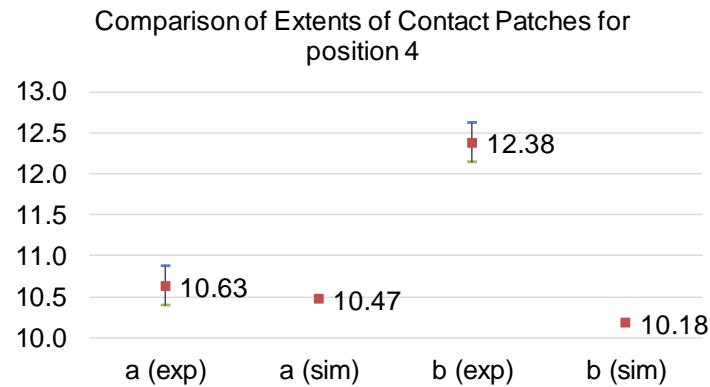


Fig. 41: Comparison of extents of contact patches obtained from simulations and experiment for position 4



## 6 Summary

The experiments were performed with a bogie loaded with dead weights on track using pressure measurement films at four different positions of wheel and rail. The contact patches for the corresponding positions were obtained. The simulations were carried out according to Design of Experiments and the results were obtained. The simulation results and the experimental results show acceptable agreement, considering the complexity of the process. There is a good match of the contact shape for positions one, two and four. For position three, desired results could not be obtained. This can be attributed to wobbling of the wheel while carrying out the experiments. Wobbling causes an increase in the angular position of the wheel with respect to rail, making the rail inclination value to move out of the chosen tolerance value. This subsequently leads to incorrect contact patches. The contact patches obtained for the other positions are continuous without any waviness. This can be attributed to smoothing of the scanned 2D profiles of the wheel and rail before the CAD geometry creation. The results imply that the pressure measurement films are appropriate for wheel-rail contact problems. The results show that for positions one, two and four, the value of extent 'a' obtained from simulations is closer to value measured in experiments and within the tolerance band. On the contrary, extent 'b', for all the positions, is invariably out of range of the experimental values. The difference between simulation and experimental value of extent 'b' for positions one, two and four is about 2.2 mm. This can be attributed to the stiffness of the wheel and rail steels and the irregularities in the wheel and rail profiles along the circumference and length respectively. One possible way to eliminate this problem could be to introduce gasket elements on the contact surface. The stiffness of these elements can be tweaked to emulate the behavior of the pressure measurement film. By this method, one can expect bigger contact area than in the steel-steel contact.

## Bibliography

- [1] LEWIS, R.; OLOFSSON, U.: Wheel-rail interface handbook. Woodhead Publishing Limited, Cambridge, 2009.
- [2] KALKER, J. J.: Transient phenomena in two elastic cylinders rolling over each other with dry friction. *Journal of Applied Mechanics*, 37, p. 677-688, 1970.
- [3] JOHNSON, K. L.: The Strength of Surfaces in Rolling Contact. In *Proceedings of the Institution of Mechanical Engineers, Part C: Mechanical Engineering Science*, 203, p. 151-163, 1989.
- [4] BOSSO, N. et al.: *Mechatronic Modeling of Real-Time Wheel-Rail Contact*. Springer, Berlin, 2013.
- [5] ANDREWS, H. I.: The contact between a locomotive driving wheel and the rail. *wear*, 2, p. 468-484, 1958/59.
- [6] POOLE, W.: The measurement of contact area between opaque objects under static and dynamic rolling conditions. in *Proceedings of conference of contact mechanics and wear of Rail/wheel systems II*, Gladwell, G. M. L.; Ghonem, H.; Kalousek, J., (editor), 1986, University of Waterloo Press, Waterloo, United Kingdom, p. 59-72, 1986.
- [7] PAU, M.; AYMERICH, F.; GINESU, F.: Ultrasonic measurements of nominal contact area and contact pressure in a wheel rail system. *Proc. Instn. Mech. Engrs, Part F: J. Rail and Rapid Transit*, 214, p. 231-244, 2000.
- [8] KNOTHE, K.; LE THE, H.: Ermittlung der Normalspannungsverteilung beim Kontakt von Rad und Schiene. *Forsch. Ing. -Wes.*, 49, p. 79-85, 1983.
- [9] TELLISKIVI, T.; OLOFSSON, U.: Contact mechanics analysis of measured wheel-rail profiles using the finite element method. *Proc. Instn. Mech. Engrs, Part F: J. Rail and Rapid Transit*, 215, p. 65-72, 2001.
- [10] PIOTROWSKI, J.; KIK, W.: A simplified model of wheel/rail contact mechanics for non-Hertzian problems and its application in rail vehicle dynamic simulations. *Vehicle system dynamics*, 46, p. 27-48, 2008.
- [11] DÖRNER, F.; BETTINGER, T.; LEKUE, J; SCHINDLER, C.: Validation of Finite Element wheel-rail contact simulations. In POMBO, J: *Proceedings of the third international conference on Railway technology: Research, Development and Maintenance*. Civil-Comp-Press, Stirlingshire, UK, paper 156, 2016.
- [12] JOHNSON, K. L.: *Contact Mechanics*. Cambridge University Press, Cambridge, 2003.

- [13] HELLEN, T. K.; BECKER, A. A.: Finite Element Analysis for Engineers- A Primer. NAFEMS, 2013.
- [14] 2D Finite Element Mesh. URL: <https://cdn.comsol.com/wordpress/2013/10/Mesh-refinement-iterations-and-computed-stress-field.png>. (visited on 15.08.2017)
- [15] 3D Finite Element Mesh. URL: [http://gmsh.info/gallery/Zylkopf3D\\_small.png](http://gmsh.info/gallery/Zylkopf3D_small.png). (visited on 15.08.2017)
- [16] WRIGGERS, P.: Non-linear Finite Element Methods. Springer, Berlin, 2010.
- [17] ANTONY, J.: Design of Experiments for Engineers and Scientists. Elsevier, 2014.
- [18] DÖRNER, F.; KÖRBLEIN, C.; SCHINDLER, C.: On the accuracy of the pressure measurement film in Hertzian contact situations similar to wheel-rail contact applications. Wear, 317, p. 241-245, 2014.
- [19] FUJIFILM: Prescale: Mono-sheet Pressure measurement film. URL: [http://www.fujifilm.com/products/measurement\\_film/en/prescale/feature](http://www.fujifilm.com/products/measurement_film/en/prescale/feature). (visited on 15.08.2017)
- [20] LEKUE, J.; DÖRNER, F.; SCHINDLER, C.: Determination of the Measurement Accuracy of the Prescale Pressure Measurement Film in the Wheel-Rail Normal Contact. In ZOBORY, I. (Editor). Proceedings of the 10th International Conference on Railway Bogies and Running Gears (Bogie '16). Budapest University of Technology and Economics (BME) and Scientific Society of Mechanical Engineers (SSME/GTE), Department of Rolling Stock, p. 149-156, 2017.
- [21] CALIPRI: Profile measurement device. URL: <http://www.ctecnologia.com.br/categoria-produto/tecnologia-metroferroviaria/medidor-de-perfis/calipri/>. (visited on 15.08.2017)
- [22] CALIPRI: Wheel Diameter measurement device. URL: <https://www.nextsense-worldwide.com>. (visited on 15.08.2017)

## List of figures

Fig. 1:	Wheel profile in contact with rail [1] .....	3
Fig. 2:	Different regions of wheel and rail profiles and wheel in new and worn States [1] .....	4
Fig. 3:	Wheel-rail contact zones [1] .....	5
Fig. 4:	Comparison between FE, CONTACT and Hertz Analysis [1] .....	6
Fig. 5:	Non-conforming surfaces in Contact [12] .....	7
Fig. 6:	Non-conforming surfaces after deformation [12] .....	10
Fig. 7:	Contact of bodies with general profile: The shape of the ellipse (b/a) and functions $F_1$ , $F_2$ and $F_3 (=F_1^{-2})$ in terms of ratio ( $R'/R''$ ) of relative curvatures [12] .....	13
Fig. 8:	FEM process flow chart .....	15
Fig. 9:	Example of a 2D and 3D FE mesh [14] [15] .....	16
Fig. 10:	Contact geometry and geometric approach [16] .....	18
Fig. 11:	Main effects and Interactions .....	23
Fig. 12:	Cross-section view of the mono-sheet pressure measurement film [19] .....	27
Fig. 13:	Experimental setup .....	28
Fig. 14:	Distance between outer edges of rail and wheel .....	29
Fig. 15:	Measured parameters in experiments .....	30
Fig. 16:	Modelling flow chart .....	32
Fig. 17:	CALIPRI profile and diameter measurement devices [21] [22] .....	33
Fig. 18:	Rail and wheel profiles measured with CALIPRI profile measurement device .....	34
Fig. 19:	Mathematical model .....	35
Fig. 20:	Discrete regions of FE model .....	36

Fig. 21: Axle model .....	37
Fig. 22: Axle mesh .....	37
Fig. 23: Wheel model topology .....	39
Fig. 24: Main wheel sub-domain geometry .....	40
Fig. 25: Main wheel sub-domain mesh.....	41
Fig. 26: Wheel sub-domain 2 geometry .....	42
Fig. 27: Mesh for Wheel sub-domain 2 .....	42
Fig. 28: Geometry of Wheel-contact surrounding area.....	44
Fig. 29: Mesh for Wheel-contact surrounding area .....	44
Fig. 30: Geometry of Wheel contact element .....	45
Fig. 31: Meshed Wheel contact element.....	46
Fig. 32: Rail model topology .....	47
Fig. 33: Main rail sub-domain model .....	48
Fig. 34: Main rail sub-model mesh .....	48
Fig. 35: Rail-contact surrounding area .....	50
Fig. 36: Mesh for Rail-contact surrounding area .....	51
Fig. 37: Geometry of Rail contact element .....	52
Fig. 38: Rail contact element mesh.....	52
Fig. 39: Comparison of extents of contact patches obtained from simulations and experiment for position 1 .....	58
Fig. 40: Comparison of extents of contact patches obtained from simulations and experiment for position 2.....	60
Fig. 41: Comparison of extents of contact patches obtained from simulations and experiment for position 4.....	63

## List of tables

Tab. 1:	Example for confounding .....	25
Tab. 2:	Example of $2^2$ full factorial design .....	26
Tab. 3:	Experiment positions and corresponding details .....	29
Tab. 4:	Details of contact patches obtained from experiments (extents with correction) ...	31
Tab. 5:	Factors with normal distribution.....	35
Tab. 6:	Boundary conditions on axle .....	38
Tab. 7:	Boundary conditions on Main wheel sub-domain .....	41
Tab. 8:	Boundary conditions on Wheel sub-domain 2 .....	43
Tab. 9:	Boundary conditions on Wheel-contact surrounding area .....	45
Tab. 10:	Boundary conditions on Wheel contact element.....	46
Tab. 11:	Boundary conditions on Main rail sub-model.....	49
Tab. 12:	Boundary conditions on Rail-contact surrounding area .....	51
Tab. 13:	Boundary conditions on Rail contact element.....	53
Tab. 14:	List of simulations for DOE.....	54
Tab. 15:	Outcomes of simulations for position 1.....	56
Tab. 16:	Details of contact patches obtained from simulations and experiment for position 1 .....	57
Tab. 17:	Outcomes of simulations for position 2.....	58
Tab. 18:	Details of contact patches obtained from simulations and experiment for position 2 .....	59
Tab. 19:	Outcomes of simulations for position 3.....	61
Tab. 20:	Outcomes of simulations for position 4.....	62

Tab. 21: Details of contact patches obtained from simulations and experiment for  
position 4 ..... 63